Nano Research

ISSN 1998-0124 CN 11-5974/O4
https://doi.org/10.26599/NR.2025.94907877

Research Article

Surface diffusion-Limited dealloying: A strategy for porosity construction in small-sized alloy nanoparticle electrocatalysts

Siming Li[1,§], Jieyu Zhang[1,§], Suizhu Pei[1], Kangjia Wu[1], Bowen Zhao[1], Min Wang[2](✉), Yawei Li[1](✉)

[1] School of Chemistry and Chemical Engineering, Shanxi University, Taiyuan 030006, China

[2] College of New Energy, China University of Petroleum (Ease China), Qingdao 266580, China

[§] Siming Li and Jieyu Zhang contributed equally to this work.

Nano Res., **Just Accepted Manuscript** • https://doi.org/10.26599/NR.2025.94907877

https://www.sciopen.com/journal/1998-0124 on Aug. 3, 2025

Just Accepted

Surface Diffusion-Limited Dealloying: A Strategy for Porosity Construction in Small-Sized Alloy Nanoparticle Electrocatalysts

Siming Li[1,†], Jieyu Zhang[1,†], Suizhu Pei[1], Kangjia Wu[1], Bowen Zhao[1], Min Wang[2]*, Yawei Li[1]*

1 School of Chemistry and Chemical Engineering, Shanxi University, Taiyuan 030006, China

2 College of New Energy, China University of Petroleum (Ease China), Qingdao 266580, China

† These authors contributed equally.

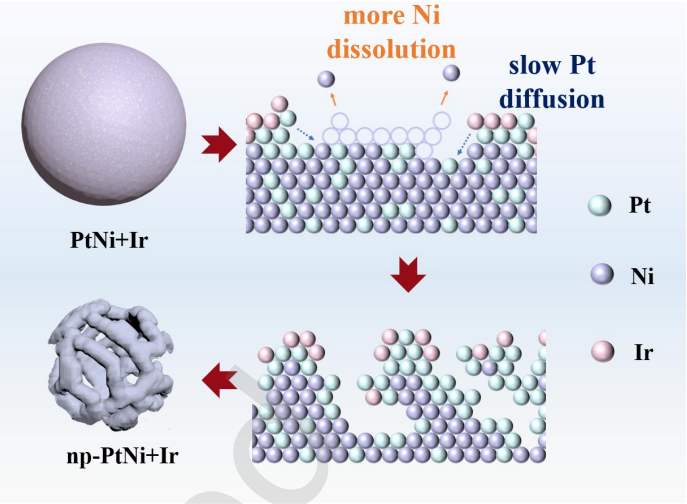

In the journey of pursuing breakthroughs in the field of materials science, this work blazes a new trail by innovatively improving the dealloying process. It exquisitely modifies the precursor nanoparticles with the exogenous metal iridium, precisely controls the dealloying process, effectively slows down the diffusion rate of platinum, drives the dissolution of more nickel, and thus prepares small-sized porous materials with unique properties, opening up a new path for the development of related fields.

Nano Research

ISSN 1998-0124 CN 11-5974/04
https://doi.org/10.26599/NR.2025.94907877

Research Article

Surface diffusion-Limited dealloying: A strategy for porosity construction in small-sized alloy nanoparticle electrocatalysts

Siming Li[1,§], Jieyu Zhang[1,§], Suizhu Pei[1], Kangjia Wu[1], Bowen Zhao[1], Min Wang[2] (✉), and Yawei Li[1] (✉)

[1] School of Chemistry and Chemical Engineering, Shanxi University, Taiyuan 030006, China
[2] College of New Energy, China University of Petroleum (Ease China), Qingdao 266580, China
[§] Siming Li and Jieyu Zhang contributed equally to this work.

Received: 14 April 2025 / **Revised:** 28 July 2025 / **Accepted:** 3 August 2025

ABSTRACT

The formation of porosity within nanoparticles via dealloying is notably constrained by the dimensions of the precursor particles, a limitation stemming from the surface kinetic processes occurring during dealloying. In this study, we present a straightforward methodology, specifically tailored for fabricating diminutive nanoporous alloy nanoparticles, originating from their small-sized precursor counterparts. We initiated our research with precursor PtNi alloy nanoparticles which possess an average diameter of 9 nm. By incorporating an extrinsic metal, Ir, known for its slower surface diffusion on the nanoparticle surface, we successfully modulated the surface migration velocity of Pt during the dealloying process of the PtNi alloy nanoparticles. This precise manipulation led to the formation of an abundantly complex nanoporous structure on diminutive PtNi nanoparticles. Owing to their enhanced high surface area-to-volume ratio and the synergistic alloy effect, electrochemical tests revealed that the Ir-coated diminutive nanoporous PtNi nanoparticles exhibit superior electrocatalytic activities towards oxygen reduction and formic acid oxidation reactions. Furthermore, the presence of Ir on the surface effectively suppresses the surface diffusion rate of Pt, thereby significantly inhibiting the coarsening evolution of the porous metallic structure. This intervention ensures the long-term preservation of both structural integrity and catalytic stability.

KEYWORDS

porous metal, dealloying, oxygen reduction reaction, formic acid oxidation reaction, coarsening

1 Introduction

Within the realm of cutting-edge material science, nanotechnology exhibits a robust and burgeoning trajectory. Nanoporous metallic materials, characterized by their distinctive microstructures, standing in stark contrast to their dense bulk counterparts, boasting an intricate network of three-dimensional bi-continuous ligaments and pores[1]. Such an architecture not only endows them with an exceptional specific surface area but also significantly enhances their reactivity[2, 3]. On this basis, their inherent metallic properties have facilitated their widespread application across a spectrum of fields, including catalysis, sensing, actuation and biomedical applications[4-9]. Nanoporous metals and alloys, with their self-supporting porous structures, possess significant advantages in electrocatalysis, owing to the combined effects of confinement, an elevated specific surface area, pronounced surface defects, and enhanced electrical conductivity[10-13]. Known with their exemplary resistance to corrosion and their outstanding performance as catalysts in electrochemical conversion technologies, Pt-based nanoporous alloys hold considerable significance, as they not only optimize the utilization of precious metal atoms to reduce production costs, but also significantly enhance catalytic efficiency and mechanical robustness[14-17].

The dealloying technique, renowned for its efficacy in creating open nanoporosity, is characterized by its simplicity and brevity in process flow. Concurrently, the method guarantees a variety of nanoporous metals while adeptly managing porosity and metal surface structures[10, 18-20]. Alternatively known as selective corrosion, the dealloying process capitalizes on the chemical reactivity disparities among alloy constituents, employing chemical or electrochemical techniques to selectively eliminate the more reactive elements, thereby enabling the residual components to spontaneously generate a three-dimensional, bicontinuous porous metal structure via atomic diffusion and aggregation[21, 22]. In the early 2000s, Erlebacher pioneered the development of an atomic model of kinetic Monte Carlo simulation depicting dealloying pore evolution, meticulously detailing the mechanisms underlying the evolution of the porous structure throughout the dealloying process[23]. Taking the AuAg alloy as an example, the process involves immersing the precursor alloy in a corrosive solution where, under a potential that exceeds the critical potential of Ag, Ag atoms continuously dissolve either within the lattice or across the surface. The more noble Au atoms, in contrast, diffuse across the surface to form a passivation region, which enables the construction a bicontinuous nanoporous alloy materials and further reducing the system's overall energy. In the case of Pt-based alloys

Address correspondence to Yawei Li, yaweili@sxu.edu.cn; Min Wang, minwang@upc.edu.cn

electrocatalysts, the dealloying process involves the dissolution of less noble component, such as Ni, while simultaneously facilitating the diffusion of Pt atoms across the alloy surface[24, 25]. This sequence of events induces geometric strain on the Pt shell, consequently enhancing the performance of the electrocatalysts[26]. Through the meticulous adjustment of dealloying conditions, alloys with either core-shell and nanoporous structures can be formed[27]. Strasser et al.[28] manipulated the formation of nanoporous PtNi alloys through the employment of a chemical dealloying technique that was meticulously regulated under oxygen conditions. The process of dealloying within an atmospheric air environment facilitated the emergence of a nanoporous architecture; conversely, within the confines of a N_2 atmosphere, a core-shell configuration was precipitated. Ding et al.[19] strategically crafted a nanoporous PtAuAg composite, featuring an ultralow Pt content in fuel cell electrode. Yang et al.[29] dedicated their research efforts to an in-depth examination of the profound effects of the corrosion process on the catalytic performance of materials. Through a series of corrosion methodologies, including electrochemical, organic acid-based (acetic acid), and strong oxidizing acid (nitric acid), they targeted the removal of the Ni-rich phase, from the rhombic dodecahedral PtNi precursor, consequently constructing a nanoscale framework. Coincidentally, Duan[30] successfully prepared nanoporous PdPt alloys with uniform ligament sizes and controllable bimetallic ratios by selectively dealloying Al from a PdPtAl ternary alloy. Meanwhile, Zhu[31] employed a dealloying process to fabricate composite nanoporous AuPt alloys with precisely predetermined compositional ratios. Both types of alloys have demonstrated significant potential in formic acid fuel cell applications. Up to now, despite the abundance of reports detailing the preparation methodologies and attendant properties of porous Pt-based alloy materials, an issue has progressively emerged concerning the limitation imposed by the nanoparticle size of the precursor alloy on the formation of porous structures during the dealloying process[32, 33]. With PtNi system serving as a case in point, Snyder et al. revealed that the critical particle size threshold for the formation of completely complex porous nanostructures is approximately 15 nm[32]. This can be attributed to the competitive dynamics that occur during the dealloying process of Pt-based alloy nanoparticles, where the leaching of transition metals is in contention with the surface diffusion of remaining Pt atoms. It is exclusively when the particle size surpasses this critical threshold will the spontaneous formation of complex nanopores ensue[32, 34]. Porosity was selectively formed in the larger particles, as the smaller ones are likely to rapidly develop a passive Pt surface layer following the depletion of the alloying component from the outermost atomic layers[32]. Therefore, within the smaller-sized alloy nanoparticles, the relatively short diffusion path of the noble component results in a fast surface passivation process, making it more likely to develop into a core-shell or multi-core-shell solid structure, while particles of larger dimensions tend to form more complex porous network structures[35]. Therefore, it is crucial to select an appropriate size distribution for fine-tuning the pore structure at the particle scale. Considering a smaller particle size inherently corresponds to a larger specific surface area, we are interested in the fabrication of small alloy nanoparticles that are capable of evolving porosity, which may necessitate diameters that are around 10 nm.

In this study, we have developed a universal and scalable dealloying strategy by introducing external metals onto the surface, modulating the surface free diffusion rate of Pt during the dealloying of PtNi alloy nanoparticles, and facilitating the fabrication of adjustable and complex nanoporous alloys with diameters significantly smaller than those of conventional particles. To elucidate this concept, we utilized the surface-liminted redox replacement (SLRR) method to deposit a foreign metallic species, specifically Ir, onto the surface, serving as a regulatory element during the dealloying process. It has been experimentally demonstrated that the addition of sub-partial monolayer of Ir impedes the step edge movement of Pt, thereby slowing the overall diffusive flux of Pt along the surface during the dealloying process, ultimately enabling the formation of complex nanoporous structures within particles as small as 9 nm in size. Moreover, attributed to their structural advantages and intricate component compositions, these smaller nanoporous PtNi nanoparticles possess robust alloy ligaments and high-density defect sites, thereby exhibiting superior active surface areas and catalytic performance, notably in the reduction of oxygen and the oxidation of formic acid.

2 Experimental section

2.1 Chemicals and reagents

Ni(Ⅱ) acetylacetonate ($Ni(acac)_2$, 95%), Pt(Ⅱ) acetylacetonate ($Pt(acac)_2$, 97%), 1-adamantanecarboxylic acid (ACA, 98%), 1,2-dichlorobenzene (DCB, 99%), 1,2-tetradecandiol (TDD, 90%), oleylamine (90%), diphenyl ether (DPE, 99%), n-hexane (C_6H_{14}, 98%), ethanol anhydrous (C_2H_6O, 99.8%), propan-2-ol (C_3H_8O, 99.95%) and carbon black were purchased from RHΛWN. Perchloric acid ($HClO_4$, 72%) was obtained from CHRON chemicals. Formic acid (HCOOH, 98%) was purchased from DM chemicals. Commercial 20% Pt/C (TKK-TEC-10EA20E) was obtained from SCI Materials Hub.

2.2 Catalyst synthesis

15nm PtNi precursor alloy nanoparticles. Alloy nanoparticles are prepared by reducing organic metal salts. In a typical synthesis for nanoparticles of approximately 15 nm in size, nickel acetylacetonate (0.8 mmol, 205.52 mg) and 1,2-tetradecanediol (0.5 mmol, 115.195 mg) are dissolved in a mixture of 4 ml oleylamine and 10 ml diphenyl ether. This mixture is then added to a 250 mL four-necked flask equipped with magnetic stirring. Throughout the experiment, the reaction system is degassed with argon to remove oxygen. The temperature is raised to 200°C, and the reaction mixture rapidly turns sky-blue under stirring. Simultaneously, a mixture of platinum acetylacetonate (0.2 mmol, 78.662 mg), 1-adamantanecarboxylic acid (3 mmol, 540.75 mg), and 3 ml of o-dichlorobenzene, pre-heated to 180°C, is quickly injected into the reaction mixture. The reaction temperature is maintained at 225°C for 1 hour. After the reaction is completed, the product is separated by centrifugation with the addition of organic solvents such as ethanol and n-hexane. Finally, the nanoparticle product is dispersed in ethanol and supported on

Vulcan XC-72R carbon at a loading of approximately 30 wt%.

9nm PtNi precursor alloy nanoparticles. For the preparation of 9nm PtNi nanoparticles, nickel acetylacetonate (0.8 mmol, 205.52 mg) and 1,2-tetradecanediol (0.5 mmol, 115.195 mg) are dissolved in a mixture of 4 ml oleylamine and 10 ml diphenyl ether. This solution is then added to a 250 mL four-necked flask equipped with magnetic stirring. Throughout the experiment, the reaction system is purged with argon to remove oxygen. The temperature is increased to 200°C, and the reaction mixture rapidly turns sky-blue under continuous stirring. Meanwhile, a mixture of platinum acetylacetonate (0.2 mmol, 78.662 mg), 1-adamantanecarboxylic acid (0.5 mmol, 90.125 mg), and 3 ml of o-dichlorobenzene, pre-heated to 200°C, is swiftly injected into the reaction mixture. The reaction temperature is maintained at 200°C for 1 hour. Once the reaction is complete, the product is separated by centrifugation after adding organic solvents like ethanol and n-hexane. Finally, the nanoparticle product is dispersed in ethanol and supported on Vulcan XC-72R carbon at a loading of approximately 30 wt%.

PtNi+Ir nanoparticles. Underpotential deposition of Cu (Cu_{UPD}) is carried out in a constant-potential mode in a solution of 1 mM $CuSO_4$ + 0.1 M H_2SO_4. The Cu-doped PtNi working electrode is transferred to a 0.01 mM $IrCl_3 \cdot xH_2O$ solution and left to stand for 10 minutes. After the galvanic displacement of Cu by Ir, the Ir-doped PtNi nanoparticles are washed with deionized (DI) water before further testing.

Dealloying of PtNi or PtNi+Ir nanoparticles. 5 mg of PtNi or PtNi+Ir nanoparticles and 5 mL of an acetic acid-ethanol solution (with a volume ratio of 1:20) are added to a scintillation vial. The mixed solution is ultrasonically treated for 5 minutes, during which the solution turns black. Subsequently, the mixture is transferred to a hydrothermal synthesis vessel equipped with a magnetic stirring rod. The solution is then stirred at 100°C for 12 hours. Afterward, the product is separated by adding ethanol to the solution and centrifuging.

2.3 Characterization

Transmission electron microscopy (TEM) and high-resolution TEM (HRTEM) were carried out on JEM-2100F operating at 200 kV. The high-angle annular dark-filed scanning TEM (HAADF-TEM) images were obtained using a Spectra Ultra S/TEM at an accelerating voltage of 300 kV. The generated elemental maps and atomic ratio of Ni to Pt in the catalysts was determined by energy-dispersive X-ray spectroscopy (EDS) (Thermo Scientific Ultra-X). Pt, Ni and Ir contents in the catalysts were quantified with inductively coupled plasma mass spectrometry (ICP-MS) using Agilent 7800 Instruments. For each sample, three duplicates were measured for accuracy with the error below 5%. Identical location TEM (IL-TEM) was used to qualitatively track the porosity evolution in nanoporous nanoparticles as a function of cycle number during accelerated durability test (ADT). A Au TEM grid (EMCN Tech) with a carbon supportive film was used as both the working electrode for ADT and material support for TEM analysis. X-ray diffraction (XRD) was carried out on a Rigaku SmartLab SE using Cu KR radiation at a step rate of 2°/min. X-ray photoelectron spectroscopy (XPS) measurements were performed on a spectrometer from Thermo Scientific K-Alpha using Al Kα radiation at a power of 72 W (6 mA, 12 kV).

2.4 Electrochemical measurements

Chemical tests were conducted in a single chamber three-electrode cell. The working electrode is a catalyst-coated glassy carbon (GC) substrate with a diameter of 5 nm. The reference electrode is an Ag/AgCl electrode (RE), and a Pt mesh is used as the counter electrode (CE). All potentials reported in this work are for reversible hydrogen electrodes (RHE). Thin-layer catalyst electrodes are prepared by mixing 5.7 mg catalyst with 4 mL aqueous solution (H_2O : IPA = 1:1) and 6 μL 5 wt% Nafion solution as binder. Sonicate the catalyst ink in an ice bath for 20 minutes and drip a suitable volume of catalyst ink with a loading capacity of 12 μg_{Pt} cm^{-2} onto the surface of the GC substrate. The films were dried under a flow of Ar.

The electrodes were subjected to an electrochemical treatment by Cyclic voltammetry (CV) between 0 V and 1.23 V at 20 mV s^{-1} in Ar-saturated 0.1 M $HClO_4$ solution. The steady recorded cycle was used to evaluate the H_{UPD}-based electrochemically active surface area ($ECSA_H$). A CO stripping voltammogram was also used to evaluate the active surface area ($ECSA_{CO}$). The irreversibly adsorbed CO layer was formed by immersing the electrode in CO-saturated 0.1 M $HClO_4$ at 0.05 V for 1 minute, followed by purging Ar into the solution for 15 minutes to remove the dissolved CO. Therefore, ECSA is integrated through the adsorbed hydrogen/carbon monoxide and further calculated according to the following formula:

$$ECSA_H = Q_H / (0.21 \times m_{Pt}) \quad (1)$$

$$\text{or } ECSA_{CO} = Q_{CO} / (0.42 \times m_{Pt}) \quad (2)$$

where Q_H or Q_{CO} (mC) denotes the charge associated with H or CO adsorption/desorption. 0.21/0.42 (mC cm^{-2}) denotes the charge associated with H/CO adsorption in a monolayer on Pt, and m_{Pt} (mg_{Pt}) denotes the actual loading of Pt on GC.

The oxygen reduction polarization curve was measured using linear sweep voltammetry (LSV). The measurement was carried out in an O_2-saturated electrolyte within a potential range from 0 V to 1.23 V, with a scan rate of 20 mV s^{-1} and a rotation speed of 1600 rpm. To correct the ORR current of the catalyst for capacitive current, the background current scanned and recorded in the Ar-saturated electrolyte was subtracted from the current measured in the O_2-saturated electrolyte. The mass activity and specific activity of the catalysts were determined at 0.9 V.

The formic acid oxidation curve was conducted in 0.1 M $HClO_4$ + 1 M HCOOH solutions with the scan rate of 50 mV s^{-1}. The mass activity and specific activity were calculated at 1.0 V vs. RHE.

ADT measurements of catalysts for 10,000 cycles have been carried out by potential cycling between 0.6 V and 1.1 V with a scan rate of 50 mV s^{-1} in 0.1 M $HClO_4$ solution under Ar atmosphere.

3 Results and discussions

3.1 Characterizations

In this study, the precursor PtNi alloy nanoparticles were synthesized via solvothermal reductive approach. Two primary factors during the synthesizing process significantly influences the final dimensions of the PtNi alloy nanoparticles[32]:the quantity of the ACA capping agent and the heating rate to

nucleation temperature after Pt precursor injection. The impact of ACA on particle size is primarily due to the formation of a monomer-ACA complex, which effectively raises the equilibrium concentration of monomers in the solution, thereby reducing monomer oversaturation. Higher concentration of ACA capping agent significantly reduces the nucleation rate, thereby enabling growth on fewer seed nuclei, ultimately resulting in larger particles.[36, 37] Moreover, maintaining an appropriate heating rate nucleation temperature is crucial for stabilizing the monomer-ACA complex in the solution, thereby ensuring consistent particle size.[37-39] Therefore, by optimizing these two parameters reasonably as indicated in the experimental section, a uniformly sized nanoparticle catalyst was successfully obtained. And the acid leaching dealloying method has been utilized on the precursor PtNi nanoparticles to obtain the desired nanoporous structure, a process that is fundamentally dependent on the continuous exposure and dissolution of underlying active metal atoms over an extended period[23, 34, 40]. Compared to Pt, Ni exhibits higher reactivity, allowing it to be preferentially leached in conventional acid solutions while preserving the diffusion of Pt atoms along the step edges[32, 41-43]. As show in Fig. 1, an appropriate corrosion time ensures the thoroughness of the dealloying process, thereby preventing structural collapse, a critical factor in maintaining the integrity of the nanoporous structure.

According to the transmission electron microscopy (TEM) images in Fig. S1(a) and S1(b), the PtNi nanoparticles are well-dispersed on the carbon support, exhibiting minimal agglomeration. Additionally, these nanoparticles exhibit a narrow size distribution and a dense appearance. Indeed, as depicted in the particle size distribution histogram, the mean diameters of these nanoparticles are approximately 9nm and 15 nm, respectively. High-resolution transmission electron microscopy (HRTEM) images of the spherical particles (Fig. S1(c) and S1(d)) further reveal distinct lattice striations. The measured lattice spacings of 0.1824/0.1930 nm and 0.2085/0.2232 nm correspond to the (200) and (111) facets of the PtNi alloy, respectively. Representative TEM and high-angle annular dark-field TEM (HAADF-TEM) images of the 9 nm nanoporous PtNi nanoparticles (denoted as 9nm-np-PtNi) after dealloying (Fig. 2(a), 2(b) and Fig. S2)) reveals the porosity evolution, where most particles contain large pores and thicken ligaments. The contrast between light and dark regions in Fig. 2(a) indicates the formation of local pores within the particles, which is accompanied by a slight decrease in particle size. Within comparation to the porous structure exhibited by the as-dealloyed 15 nm PtNi nanoparticles (denoted as 15nm-np-PtNi) (Fig. S3), which demonstrate a more complex porosity with thin ligaments, the partial porous of 9nm-np-PtNi can be attributed to the rapid coverage of smaller alloy nanoparticles by Pt due to the swift migration rate of Pt atoms, findings that align with prior research[32]. The 9nm-np-PtNi nanoparticles display a uniform elemental distribution of Pt and Ni, as evidenced by X-ray energy dispersive spectroscopy (EDS) (Fig. 2(c) and 2(d)), confirming the successful dealloying process and the retention of a homogeneous alloy structure. The approximately compositional ratio of Ni:Pt after dealloying for 9nm-np-PtNi (0.75:1) is higher than that for 15nm-np-PtNi (0.4:1) as indicated in Table S1. The higher residue Ni atomic composition in 9nm-np-PtNi can be attributed to the rapid completion of dealloying, during which less Ni was dissolved (Fig. S4).

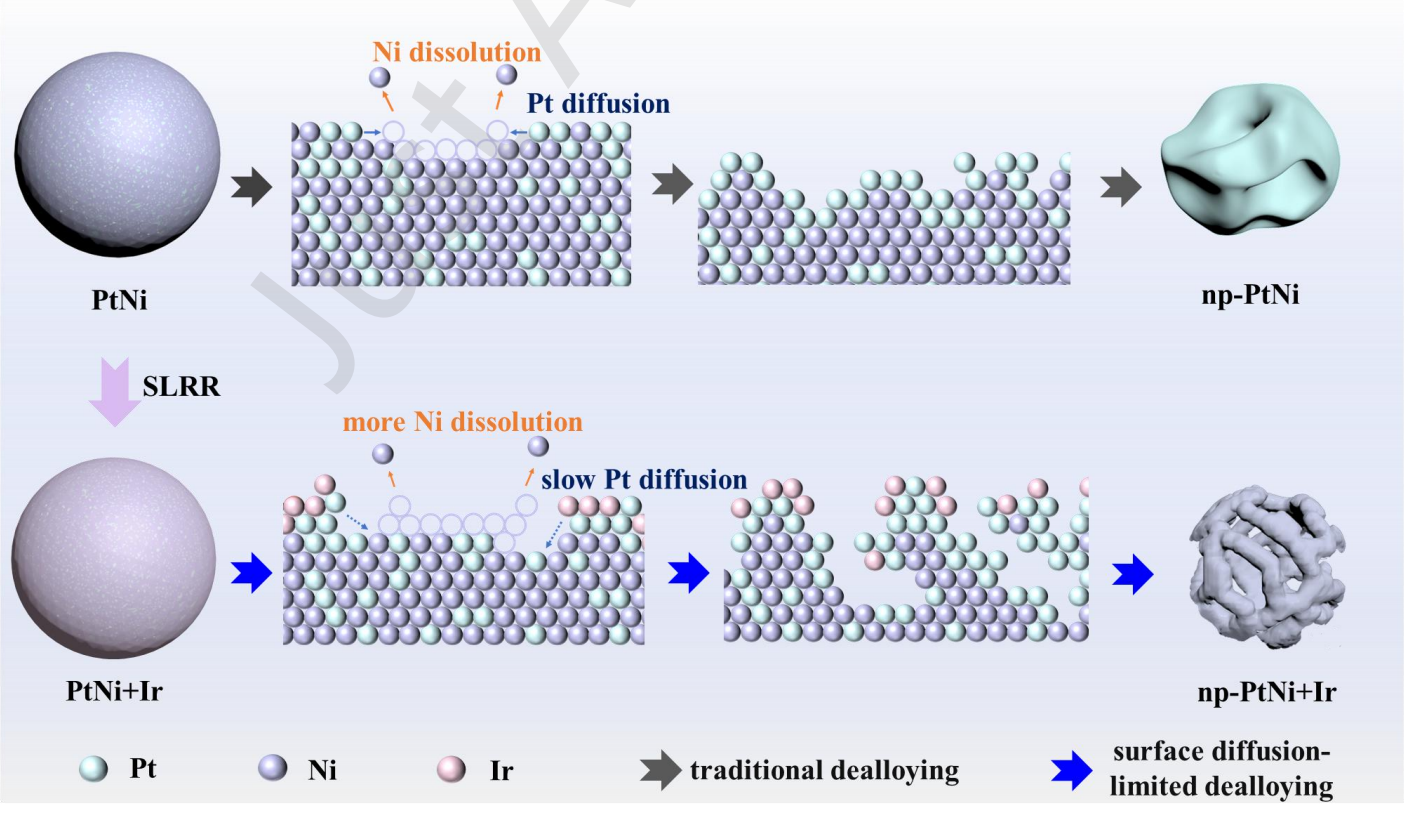

Fig. 1 Schematic illustration of dealloying for small-sized porous nano-alloys.

Nano Research
ISSN 1998-0124 CN 11-5974/04
https://doi.org/10.26599/NR.2025.94907877

Based on the fundamental theory of metal diffusion, the diffusion capacity of zero valent metals is directly related to their melting point temperature. And this correlation can be quantified by the ratio of temperature to melting point, which is T/Tm, where Tm is the melting point temperature of the metal[44, 45]. At room temperature and pressure, due to its high melting point, the diffusion behavior of Ir is relatively slow. Specifically, the chemical diffusion coefficient of Ir is about two orders of magnitude lower than that of Pt, a difference that has been demonstrated in surface self-diffusion measurements under high vacuum conditions[45-47]. Therefore, the surface doping of Ir onto precursor PtNi nanoparticles, which were effectively prepared for dealloying, reveals the correlation between the Ni etching rate and the Pt surface diffusion rate. This correlation is a crucial factor in enabling relatively small PtNi alloy particles to form highly porous structures through chemical dealloying. A partial monolayer of Ir is uniformly dispersed on the surface of PtNi nanoparticles via the surface-limited redox replacement (SLRR) method[48-50], which entails the galvanic displacement of underpotentially deposited Cu on the surface of the as-prepared PtNi nanoparticles. Notably, SLRR is a well-established procedure commonly employed for the formation of precious metal skins on metallic core nanoparticles[48, 51]. Specifically, the replacement of Cu^{2+} with Ir^{3+} results in a partial monolayer coverage, with Ir preferentially located at lower-coordinated defects on the surface, thereby effectively passivating the sites on the step edges[50]. Interestingly, as depicted in the TEM image in Fig. 2(e), the Ir-doped 9nm PtNi nanoparticles, following the dealloying process (denoted as 9nm-np-PtNi+Ir), exhibit a distinct black skeleton, which signifies the formation of a complex inter-crosslinked network structure, whereas the bright areas correspond to hollow pores embedded within the nanoskeleton. Fig. 2(f)-2(i) present the typical HAADF-TEM and EDS images of the 9nm-np-PtNi+Ir nanoparticle, revealing a more intricate and finer pore structure with thin ligaments distributed within the nanoparticles, as opposed to the non-permeable pore structure observed in 9nm-np-PtNi (Fig. S5). Notably, the porosity structure of 9nm-np-PtNi+Ir bears a striking resemblance to the intricate, interconnected spong-like porous architecture of 15nm-np-PtNi (Fig. S3), which used larger-sized particles for dealloying. Moreover, as indicated in Fig. S4 and Table S1, it is interesting to note that, in the presence of Ir, the residue Ni atomic composition of 9nm-np-PtNi+Ir is significantly lower than that of 9nm-np-PtNi, approaching that of 15 m-np-PtNi. This suggests that Ir contributes to mitigating the completion of surface passivation during the dealloying by restricting the surface diffusion of Pt. Additionally, the corresponding elemental mapping (Fig. 2(i)) clearly shows the uniform distribution of Ir following dealloying, and ICP-MS analysis confirms that Ir retention remains nearly unchanged after dealloying. (Table S2). These results highlight the stability and longevity of Ir throughout the specific dealloying procedure.

The crystal structures of 9nm-PtNi and 9nm-PtNi+Ir, pre- and post-dealloying, were examined via XRD (Fig. S6). As summarized in Table S3, a slight lattice expansion from 3.610 Å (9nm-PtNi) to 3.614 Å (9nm-PtNi+Ir) confirms successful Ir incorporation into the lattice. Post-dealloying, the 9nm-PtNi sample exhibited a significant lattice expansion to 3.702 Å, accompanied by Full Width at Half Maximum (FWHM) broadening from 1.06° to 3.55° at the (111) peak, indicating Ni leaching that transforms the single FCC phase into a Pt-rich defective structure. Conversely, 9nm-PtNi+Ir showed minimal changes in lattice parameter (3.614 Å to 3.653 Å, and FWHM (1.18 ° to 2.82 °) after dealloying, demonstrating that Ir suppresses dealloying kinetics by reducing microstrain and defect formation. These results robustly support dealloying-driven Ni dissolution in PtNi particles, while Ir mitigates this process via domain stabilization.

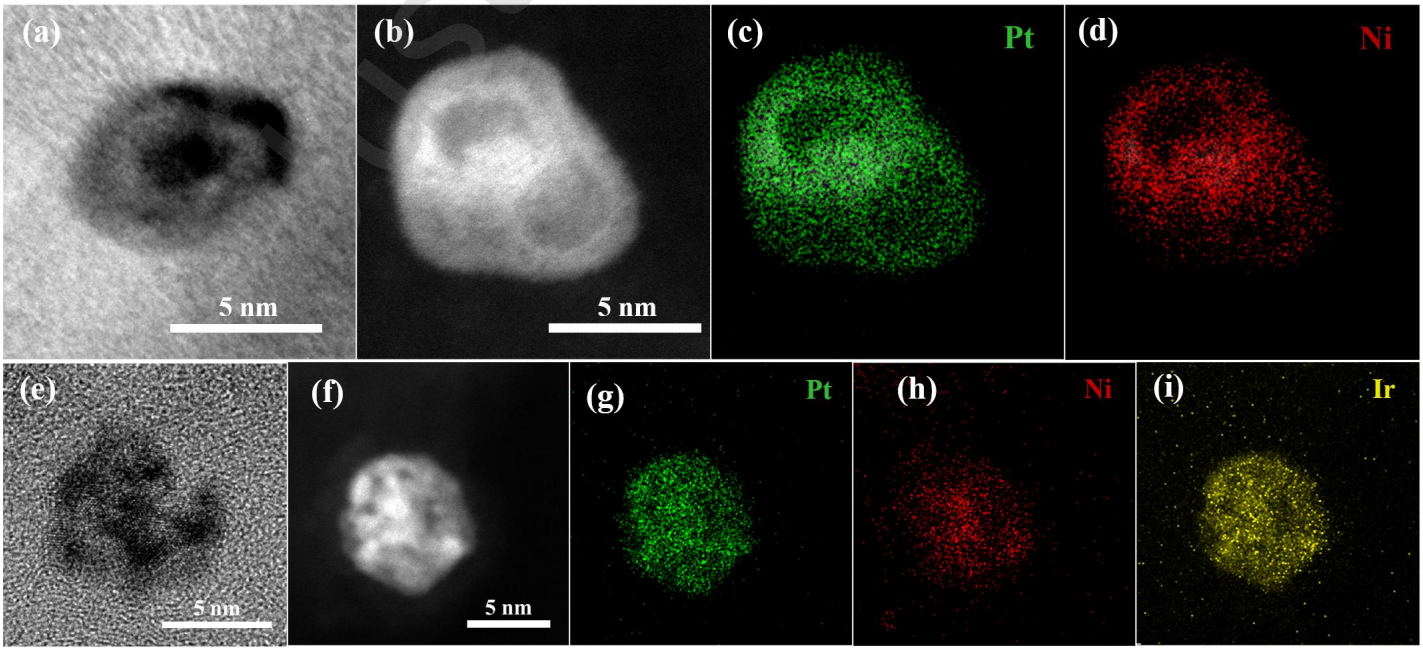

Fig. 2 (a) TEM image, (b) HAADF-TEM image and the corresponding EDS mapping of (c) Pt and (d)Ni for the sample of

9nm-np-PtNi. (e) TEM image, (f) HAADF-TEM image and the corresponding EDS mapping of (g) Pt, (h)Ni and (i)Ir for the sample of 9nm-np-PtNi+Ir.

3.2 Electrochemical performances

To evaluate the effect of Ir doping on porosity evolution towards electrocatalytic performance, electrochemical active surface area (ECSA) was first assessed through electro-oxidation of both underpotentially adsorbed hydrogen (H_{UPD}) and underpotentially adsorbed carbon monoxide (CO_{UPD}). The complex nanoporous structures are expected to provide large specific areas, and ECSA measurements were conducted to confirm this. As shown in Fig. 3(a) and 3(b), the charges of both H_{UPD} and CO_{UPD} indicate that 9nm-np-PtNi+Ir has higher Pt surface area than that of the 9nm-np-PtNi. Fig. 3(c) presents the ECSA measurement results for both. As the less-noble metal in alloying Pt alters the adsorption properties of the alloy, the ECSA determined using CO_{UPD} ($ECSA_{CO}$) gives more accurate result about the surface properties than the ECSA using H_{UPD}[52]. The difference in CO adsorption potentials may arise from changes in the surface atomic arrangement during the dealloying process. Different crystal surface orientations, such as the (111) and (100) facets, exhibit varying surface roughness, which leads to differences in CO adsorption potentials[53]. In this study, the $ECSA_{CO}$ of 9nm-np-PtNi+Ir is 44.23 $m^2\ g_{Pt}^{-1}$, which is significantly higher than that of the 9nm-np-PtNi (35.74 $m^2\ g_{Pt}^{-1}$). The higher ECSA of 9nm-np-PtNi+Ir can be attributed to its topologically complex nanostructures with high radii of curvature, while the curvature gradients are relatively lower in 9nm-np-PtNi.

Researchers have proven that alloying with transition metals such as Ni can manipulate the electron structure of Pt-based catalysts, significantly improving their electrocatalytic performances in oxygen reduction reaction (ORR) and formic acid oxidation reaction (FAOR)[54, 55]. To further confirm the role of Ir-doping during the dealloying towards the electrocatalytic performance, ORR and FAOR were performed using 9nm-np-PtNi+Ir along with 9nm-np-PtNi, and a commercially available Pt/C (TKK-TEC-10EA20E). ORR tests were carried out in an O_2-saturated 0.1 M $HClO_4$ solution. Fig. 3(d) shows the polarization curves of the three catalysts. Among all the catalysts tested here, 9nm-np-PtNi+Ir exhibits the highest ORR activity, with the half-wave potential ($E_{1/2}$) of 0.93 V, which is 50 mV and 19.76 mV more positive than Pt/C and 9nm-np-PtNi. Such superior catalytic performance can stem from the large specific surface area (Fig. 3(c)) rather than the incorporation of Ir. The improved ECSA approaches that of the optimized commercial Pt/C catalysts (Fig. S7), indicating enhanced electrochemical surface accessibility with such complex porous structures. As shown in Fig. S8, the catalytic activity of Pt/C+Ir is remarkably poor compared to that of Pt/C. Ir oxide species can be generated at relatively low potential. The oxide layer on the surface weakens the binding affinity with oxygen, thereby leading to inferior active in ORR[56]. To further assess the ORR performance of 9nm-np-PtNi+Ir, Tafel slopes are derived from LSV curves, as depicted in Fig. 3(e). The electrode of 9nm-np-PtNi+Ir exhibits the smallest slope at low overpotentials (57.91 mV dec^{-1}) compared to 9nm-np-PtNi (76.34 mV dec^{-1}) and Pt/C (86.68 mV dec^{-1}). This suggests that 9nm-np-PtNi+Ir facilitate a more rapid kinetic process and superior ORR catalytic performance. The kinetic current is calculated from the Koutecky–Levich (K–L) equation at 0.9 V vs RHE. The specific activity of 9nm-np-PtNi+Ir reaches 2.15 mA cm_{Pt}^{-2}, which is far superior to that of Pt/C (0.05 mA cm_{Pt}^{-2}) and 9nm-np-PtNi (1.48 mA cm_{Pt}^{-2}), as shown in Fig. 3(f). Additionally, owning its increased density of active sites of the porous microstructure by dealloying, 9nm-np-PtNi+Ir has a high mass activity of 0.95 A mg_{Pt}^{-1}, nearly 4 and 2 times that of Pt/C (0.25 A mg_{Pt}^{-1}) and 9nm-np-PtNi (0.53 A mg_{Pt}^{-1}), respectively.

Nano Research
ISSN 1998-0124 CN 11-5974/04
https://doi.org/10.26599/NR.2025.94907877

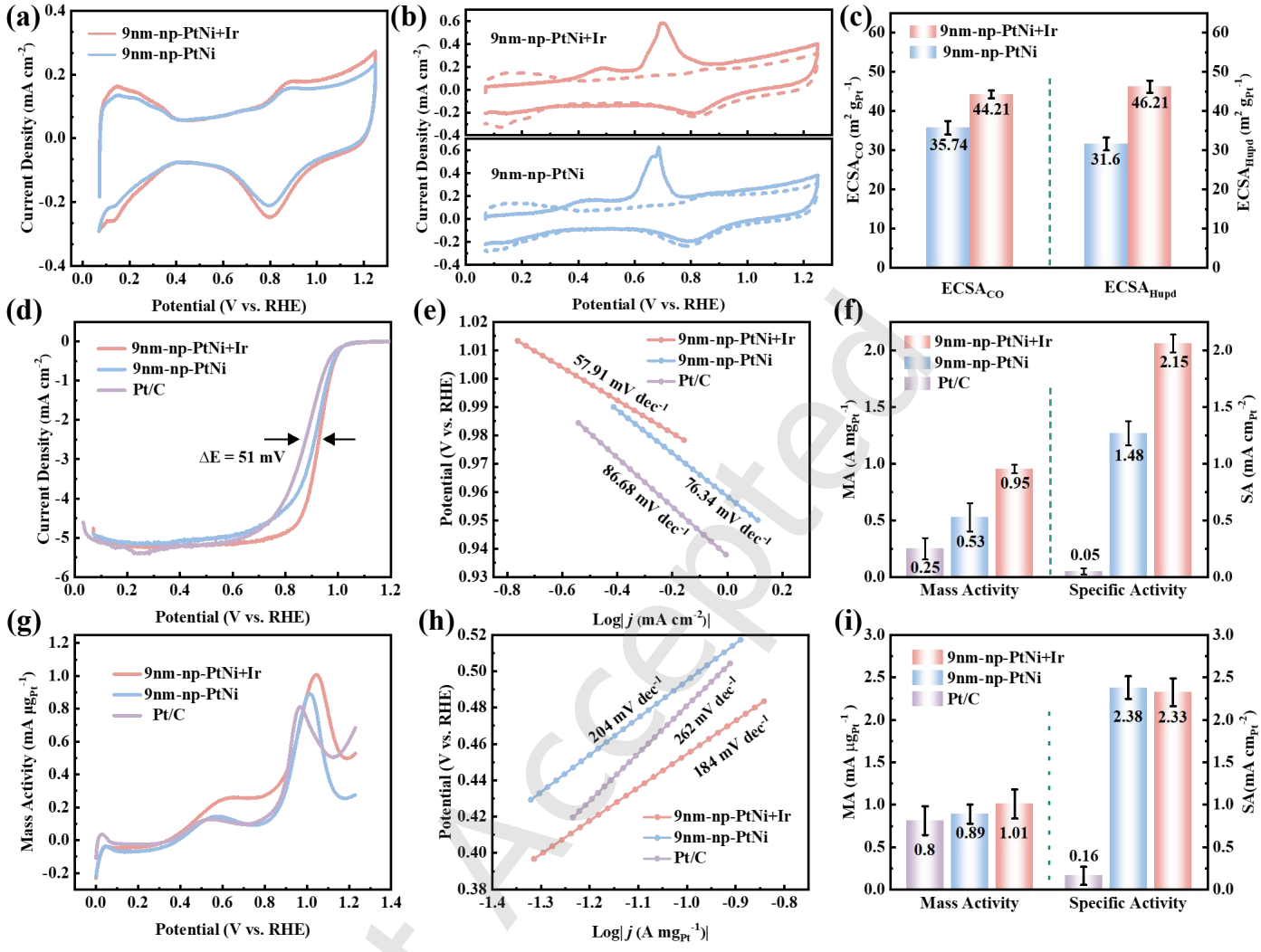

Fig. 3 (a) CV curves in Ar-saturated 0.1 M $HClO_4$, (b) the CO stripping curves of catalysts in 0.1 M $HClO_4$ and (c) ECSA of 9nm-np-PtNi+Ir and 9nm-np-PtNi. (d)ORR polarization curves in O_2-saturated 0.1 M $HClO_4$,(e) the Tafel slope and (f) Pt mass activity and specific activity at +0.9 V for ORR of 9nm-np-PtNi+Ir , 9nm-np-PtNi and Pt/C. (g) Pt mass-normalized curves of LSV toward FAOR, (h)the Tafel slope and (i) Pt mass activity and specific activity at the II oxidation peak for FAOR of 9nm-np-PtNi+Ir , 9nm-np-PtNi and Pt/C.

This newly prepared nanoporous PtNi alloy nanoparticles can also be suitable as electrocatalysts for FAOR which is an anodic reaction of significant commercial interest as it is used in direct formic acid fuel cells[57-59]. In general, formic acid electrooxidation is thought to occur via two different pathways: direct (DRP) and indirect (IDRP). Direct oxidation forms CO_2 via dehydrogenation and oxidation of the reaction intermediate. The indirect reaction pathway involves the dehydration of formic acid to produce CO. Depending on the applied potential, CO may poison the electrode or further oxidize to produce CO_2[60-62].

Direct pathway: $HCOOH \rightarrow CO_2 + 2H^+ + 2e^-$

Indirect pathway: $HCOOH \rightarrow CO_{ads} + H_2O \rightarrow CO_2 + 2H^+ + 2e^-$

The dehydrogenation of the Pt-based catalyst usually takes place at a relatively low potential[63, 64]. The magnitude of the direct current peak generated under the potential region of the anodic peak (I) is indicative of the surface catalytic activity associated with the direct electro-oxidation of formic acid. As the potential increases gradually, the predominant reaction that occurs is dehydration. The value of the indirect current peak, which is generated within the potential region of the anodic peak (II), characterizes the surface poisoning caused by the CO adsorption process. CO intermediates can be slowly oxidized when the potential exceeds a certain threshold value[65]. In the mass-normalized CV curves (Fig. S9), it is observed that all catalysts exhibit hydrogen adsorption/desorption peaks within the 0-0.3 V vs. RHE potential range. Based on the CO stripping curves of different catalysts (Fig. S10), the ECSA of 9nm-np-PtNi+Ir is calculated to be 43.54 $m^2\ g_{Pt}^{-1}$, which is higher than that of 9nm-np-PtNi (37.21 $m^2\ g_{Pt}^{-1}$). The higher ECSA can be reasonably attributed to its complex porous morphology characteristics, which inevitably elevate the surface Pt active site content. In the FAOR investigation, all measurements were completed at room

temperature in a solution containing 0.1 M $HClO_4$ + 0.5 M HCOOH. The forward scan CV curve reveals two oxidation peaks located at approximately 0.6 and 1.0 V vs. RHE, which correspond to the direct and indirect pathways, respectively (Fig. 3(g)).

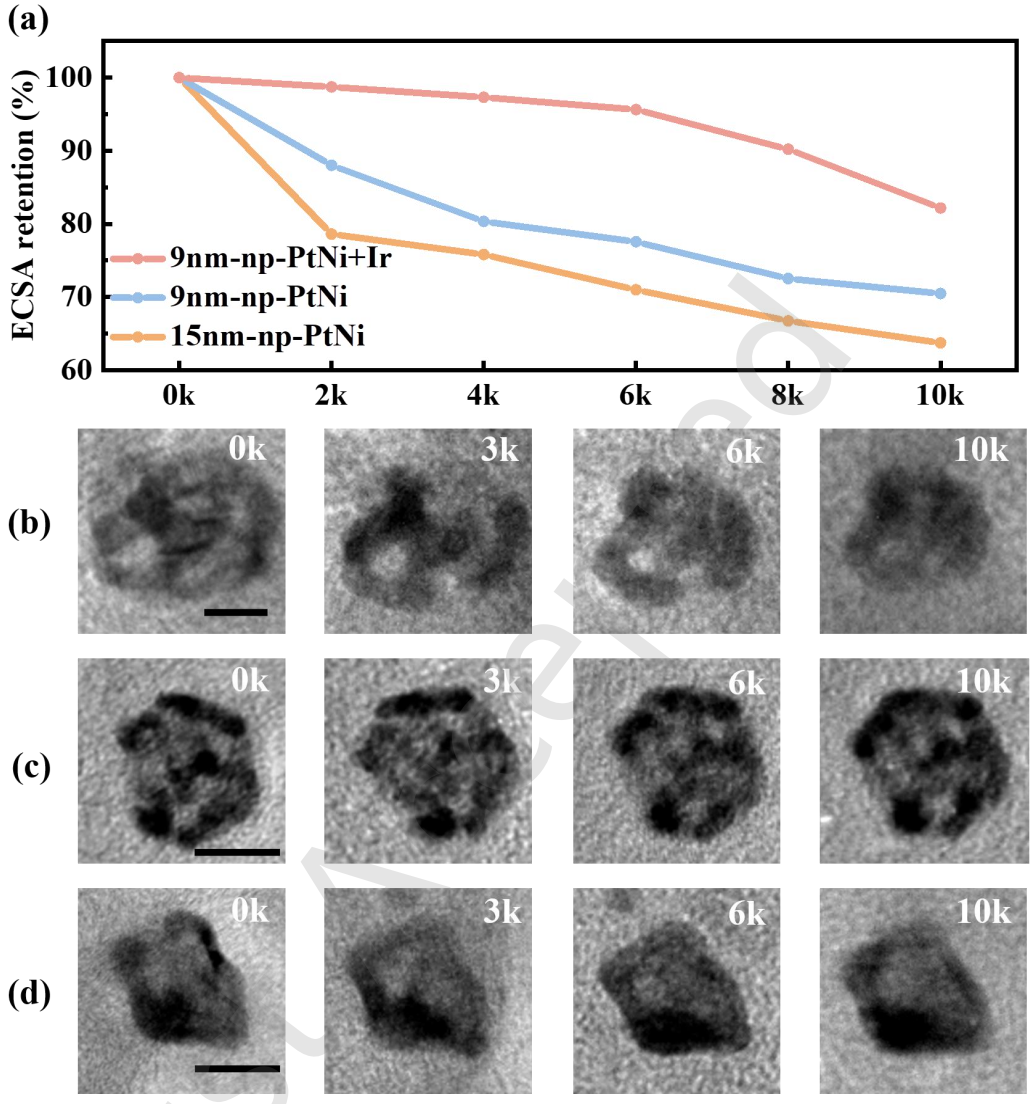

Fig. 4 (a) ECSA percentage change after 10,000 cycles of 9nm-np-PtNi+Ir, 9nm-np-PtNi and Pt/C. IL-TEM images of single (b) 15nm-np-PtNi particle, (c) 9nm-np-PtNi+Ir particle and (d) 9nm-np-PtNi particle particles during ADT. TEM images from left to right represent 0k, 3k, 6k, and 10k potential cycles. Scale bar is 5 nm.

It is worth noting that minor Ir doping minimally influences the electronic contributions to reaction kinetics. As shown in Fig. S11, 9nm-np-PtNi+Ir exhibits negligible peak shift and area ratio change in binding energy compared to the 9nm-np-PtNi reference, indicating minimal electronic perturbation from the presence of Ir. This is further supported by the nearly identical CO oxidation peak position observed with and without Ir on the surface of Pt. Therefore, Ir atoms primarily serve as diffusion barriers that promote high surface area-to-volume morphology, rather than acting as electronic structure modifiers in the ORR and MOR process.

All catalysts studied exhibit two distinct reaction trends. The catalytic activity of 9nm-np-PtNi+Ir (0.26 A mg_{Pt}^{-1}) is the highest at 0.6 V vs. RHE, being 2.2 times higher than that of Pt/C (0.12 A mg_{Pt}^{-1}). This trend is also evident at higher potential (1 V vs. RHE). This suggests that the complex porous PtNi alloy nanoparticles modified with exogenous metal Ir are the optimal choice for FAOR. As previously reported, the introduction of Ni and its unique three-dimensional structure significantly enhances FAOR activity[58]. Furthermore, the incorporation of Ir enhances the CO tolerance of the catalyst. Specifically, the electron density on the Ir surface can effectively modulate the metal-reactant interaction, thereby reducing the CO adsorption energy on the metal surface[66, 67]. As shown in Fig. 3(h), the Tafel slopes indicate that all three catalysts exhibit a strong linear relationship in the lower potential range. Notably, the slope value of 9nm-np-PtNi+Ir (184 mV dec^{-1}) is significantly lower than that of the other two catalysts. On the one hand, a high ECSA implies an abundance of highly active sites, which allows for higher current densities to be achieved at lower overpotentials. On the other hand, the open cross-linked pores facilitate the rapid transfer of

reactants and products, reducing mass transfer limitations[68]. Fig. 3(i) illustrates the values of the II oxidation peaks, normalized by Pt loading and ECSA, for formic acid over different catalysts. The specific activity (2.32 mA cm_{Pt}^{-2}) and mass activity (1.0 mA μg_{Pt}^{-1}) of 9nm-np-PtNi+Ir is 14.5 times and 1.25 times higher than those of the commercial Pt/C (0.16 mA cm_{Pt}^{-2} and 0.8 mA μg_{Pt}^{-1}), respectively. Furthermore, the current density ratio (I/II) can indirectly reflect the contribution of DRP in the FAOR process. The I/II ratio of 9nm-np-PtNi+Ir (I/II = 0.26) is larger than that of 9nm-np-PtNi (I/II = 0.16) and Pt/C (I/II = 0.15) (Fig. S12). Therefore, 9nm-np-PtNi+Ir prefers to directly oxidize the formic acid. The formation of PtNi alloys alters the electronic structure of the Pt surface, which may reduce the activation energy of the formic acid dehydrogenation step, thereby promoting the selection of direct pathway[69]. Moreover, the porous structure of the catalyst provides an effective transport pathway for intermediates, such as formate, thereby facilitating efficient transfer between active sites and enhancing overall catalytic FAOR performance[70].

The electrocatalytic durability of the catalysts was evaluated through an accelerated durability test (ADT) conducted in an Ar-saturated 0.1 M $HClO_4$ solution, spanning a potential range of 0.6 to 1.1 V vs. RHE at a scanning rate of 50 mV s^{-1}. As shown in Fig. 4(a), the change in ECSA throughout the entire ADT process was monitored via the CO stripping method. After 10,000 cycles, the $ECSA_{CO}$ of 9nm-np-PtNi+Ir exhibits a final loss of 18% compared to the initial value, while Pt/C demonstrates a substantial decay of 82%, succeeded by 9nm-np-PtNi (30%) and 15nm-np-PtNi (37%). The two common mechanisms attributed to the ECSA loss of solid nanoparticulate electrocatalysts are agglomeration/sintering[71, 72] and dissolution/Ostwald ripening[73, 74]. For three-dimensional, morphologically and topologically complex metallic materials, an additional mechanism of material degradation exists[75]. Porous materials perpetually exist in a state of meta-stability, and due to their high surface-to-volume ratios, the thermodynamic tendency to reduce this ratio drives a process known as coarsening[75]. Coarsening, which can be linked to surface smoothening, is propelled by surface diffusion currents that are proportional to gradients in the local chemical potential[76].

Fig. 4(b-c) presents identical location TEM (IL-TEM) images of three groups nanoparticles at different stages of ADT. From this series of IL-TEM images, it is evident that all the samples exhibit varying degrees of coarsening after prolonged potential cycling. Among them, the structural changes in the 15nm-np-PtNi nanoparticles (Fig. 4(b) and Fig. S13) are the most pronounced, consistent with expectations[77-79]. At the microscopic scale, large-sized porous catalytic materials are highly susceptible to the curvature minimization effect. Surface atom diffusion triggers pore contraction and coalescence, leading to the gradual degradation of the originally intricate three-dimensional porous topology, eventually evolving into a simpler porous morphology or even approaching a solid structure. In contrast, the overall structures of the 9nm-np-PtNi+Ir and 9nm-np-PtNi nanoparticles remained relatively stable. While the presence of a partial monolayer of Ir on the surface of the nanoporous nanoparticles, the structural stability was enhanced, Fig. 4(c) and Fig. S14. Although similar degradation mechanisms persisted in this system, the slower-moving dopant species (such as Ir) act to pin step edges, effectively preventing surface atomic movement and limiting the rate and degree of coarsening[75, 80], thereby maintaining the relative stability of the nanoparticle structure. Furthermore, analysis of the structural evolution of the 9nm-np-PtNi nanoparticles (Fig. 4(d) and Fig. S15) reveal a gradual trend toward spherical transformation at the nanoparticle edges. However, due to their relatively small curvature radius and higher activation energy barrier for surface atom diffusion, the rate of surface atom moving is limited. As a result, the extent of change under the same conditions is less significant compared to the 15nm-np-PtNi nanoparticles. Overall, it can be deduced that the introduction of Ir can limit Pt surface diffusion, thereby improving the stability of three-dimensional porous electrocatalytic metallic nanomaterials.

To objectively evaluate nanoparticle porosity evolution, an automated image processing protocol using Avizo software was implemented. Original TEM micrographs (Fig. 4b-4d) underwent pixel-wise segmentation through adaptive thresholding algorithms, generating binary images distinguishing solid (blue) and void (black) phases (Fig. S16). As summarized in Table S4, before ADT, 9nm-np-PtNi+Ir exhibited comparable porosity (38.7%) to unmodified 15nm-np-PtNi (36.9%), both of which significantly surpassed the porosity of the unmodified 9nm-np-PtNi (25.3%). This demonstrates that Ir's pinning effect compensates for size-dependent porosity limitations by restricting Pt diffusion during dealloying. Following ADT, 15nm-np-PtNi underwent substantial morphological coarsening, resulting in a decreased porosity of 19.1%. The porosity of 9nm-np-PtNi also decreased to 18.3%, whereas 9nm-np-PtNi+Ir retained a substantially higher porosity (32.5%). The calculated porosity evolution aligns with the ECSA degradation (Fig. 4a), further confirming that Ir atoms function as kinetic diffusion barriers, effectively suppressing ligament coalescence and preserving a high surface-to-volume morphology.

3.3 Future directions

While Ir demonstrates unique multifunctional advantages, such as acting as a diffusion barrier to create complex porosity and enhance structural stability, future studies will explore Ir-X bimetallic modifications (X = Au, Pd) where synergistic effects may enable property tuning. Element screening protocols must prioritize both kinetic diffusion rates and electrochemical stability – a combinatorial constraint uniquely satisfied by Ir under current reaction conditions.

4 Conclusions

A straightforward and rapid synthesis is developed for the preparation of small particle size porous nano-alloy catalysts. By partially depositing Ir on the surface of the PtNi precursor, the surface diffusion of Pt is hindered during the dealloying process, thereby promoting the formation of complex porous morphologies and results in a high specific surface area. Moreover, the nanoparticles are electrochemically active to reduce oxygen and formic acid molecules with higher MA and SA than commercial Pt/C. Owing to the enhanced high surface area-to-volume ratio and the synergistic alloy effect of small

nanoporous PtNi nanoparticles, the electrocatalysts exhibit superior electrocatalytic activities towards oxygen reduction and formic acid oxidation reactions. Furthermore, the presence of Ir on the surface effectively suppresses the surface diffusion rate of Pt during electrocatalytic process, thereby significantly inhibiting the coarsening evolution and increasing the stability of the porous metallic structures. The result presented here provides a development approach for preparing high-performance, smaller-sized porous alloy materials through electrochemical dealloying.

Acknowledgements

The work was financially supported by National Natural Science Foundation of China (22202124, UA22A20429), Shanxi Scholarship Council of China (2023-008, 2023-009), Shanxi Outstanding Project Selection and Support Program for Overseas Scientific and Technological Activities (20230002), Science and Technology Innovation Teams of Shanxi Province (202304051001023), and the Key Research and Development Program of Shanxi Province (No. 202302060301009), Qingdao New Energy Shandong Laboratory Open Project (QNESL OP), Shandong Provincial Natural Science Foundation (Nos. ZR2024QB175, ZR2023LFG005), and Fundamental Research Funds for the Central Universities (No. 25CX07002A)

Electronic Supplementary Material: Supplementary material (further details for TEM and HRTEM of 9nm-PtNi and 15nm-PtNi; TEM of 9nm-np-PtNi; HRTEM, HAADF-TEM and EDS elemental mapping of 15nm-np-PtNi; cyclinic voltammograms; IL-TEM of reported catalysts after stability test) is available in the online version of this article at https://doi.org/10.26599/NR.2025.94907877.

References

[1] Ding, Y.; Zhang, Z. Introduction to nanoporous metals. In *Nanoporous metals for advanced energy technologies*. 2016; pp 1-35.

[2] Guari, Y. Advanced porous nanomaterials: Synthesis, properties, and applications. *Nanomaterials*. **2024**, *14*, 1602.

[3] Wang, Y.;Yu, B.;He, M.;Zhai, Z.;Yin, K.;Kong, F.; Zhang, Z. Eutectic-derived high-entropy nanoporous nanowires for efficient and stable water-to-hydrogen conversion. *Nano Research.* **2022**, *15*, 4820-4826.

[4] Bai, Q.;Wang, Y.;Tan, F.; Zhang, Z. Eutectic-derived synthesis of hierarchically nanoporous copper for electrochemical actuation and solar steam generation. *Nano Research.* **2024**, *17*, 2011-2018.

[5] Zeng, H.;He, S.;Hosseini, S. S.;Zhu, B.; Shao, L. Emerging nanomaterial incorporated membranes for gas separation and pervaporation towards energetic-efficient applications. *Advanced Membranes.* **2022**, *2*, 100015.

[6] Du, A.;De Eulate, E. A.; Hariz, A. Design and fabrication of glucose biosensors based on immobilization of glucose oxidase on titanium oxide nanotube arrays. *J Nanosci Nanotechnol.* **2021**, *21*, 4605-4614.

[7] Zhou, X.;Xu, W.;Liang, Y.;Jiang, H.;Li, Z.;Wu, S.;Gao, Z.;Cui, Z.; Zhu, S. Dynamically restructuring nanoporous Cu–Co electrocatalyst for efficient nitrate electroreduction to ammonia. *ACS Catalysis.* **2024**, *14*, 12251-12259.

[8] Chen, Q.;Ding, Y.; Chen, M. Nanoporous metal by dealloying for electrochemical energy conversion and storage. *MRS Bulletin.* **2018**, *43*, 43-48.

[9] Guan, H.;Zhang, J.;Liu, Y.;Zhao, Y.; Zhang, B. Rapid quantitative determination of hydrogen peroxide using an electrochemical sensor based on PtNi alloy/CeO_2 plates embedded in n-doped carbon nanofibers. *Electrochimica Acta.* **2019**, *295*, 997-1005.

[10] Sang, Q.;Hao, S.;Han, J.; Ding, Y. Dealloyed nanoporous materials for electrochemical energy conversion and storage. *EnergyChem.* **2022**, *4*, 100069.

[11] Zhang, X.;Yang, Y.;Liu, Y.;Jia, Z.;Wang, Q.;Sun, L.;Zhang, L.-C.;Kruzic, J. J.;Lu, J.; Shen, B. Defect engineering of a high-entropy metallic glass surface for high-performance overall water splitting at ampere-level current densities. *Advanced Materials*. **2023**, *35*, 2303439.

[12] Kang, Y.;Cretu, O.;Kikkawa, J.;Kimoto, K.;Nara, H.;Nugraha, A. S.;Kawamoto, H.;Eguchi, M.;Liao, T.;Sun, Z.;Asahi, T.; Yamauchi, Y. Mesoporous multimetallic nanospheres with exposed highly entropic alloy sites. *Nature Communications.* **2023**, *14*, 4182.

[13] Jing, T.;Zhang, N.;Zhang, C.;Mourdikoudis, S.;Sofer, Z.;Li, W.;Li, P.;Li, T.;Zuo, Y.; Rao, D. Improving C–N–FeO_x oxygen evolution electrocatalysts through hydroxyl-modulated local coordination environment. *ACS Catalysis.* **2022**, *12*, 7443-7452.

[14] Kloke, A.;von Stetten, F.;Zengerle, R.; Kerzenmacher, S. Strategies for the fabrication of porous platinum electrodes. *Advanced Materials.* **2011**, *23*, 4976-5008.

[15] Xu, Y.; Zhang, B. Recent advances in porous Pt-based nanostructures: Synthesis and electrochemical applications. *Chemical Society Reviews.* **2014**, *43*, 2439-2450.

[16] Maiyalagan, T.; Saji, V. S. *Electrocatalysts for low temperature fuel cells*, 2017.

[17] Li, T.;Jing, T.;Jia, X.;Guo, S.;Li, W.;Yue, H.; Luo, Z. Galvanic replacement mediated 3D porous PtCu nano-frames for enhanced ethylene glycol oxidation. *Chemical Communications*. **2019**, *55*, 14526-14529.

[18] Wang, T.;Chutia, A.;Brett, D. J. L.;Shearing, P. R.;He, G.;Chai, G.; Parkin, I. P. Palladium alloys used as electrocatalysts for

the oxygen reduction reaction. *Energy & Environmental Science.* **2021**, *14*, 2639-2669.

[19] Wen, X.;Yin, S.;Yin, H.; Ding, Y. A displacement dealloying route to dilute nanoporous PtAu alloys for highly active formic acid electro-oxidation. *Electrochimica Acta.* **2021**, *373*, 137884.

[20] Wang, R.;Xu, C.;Bi, X.; Ding, Y. Nanoporous surface alloys as highly active and durable oxygen reduction reaction electrocatalysts. *Energy & Environmental Science.* **2012**, *5*, 5281-5286.

[21] Chuang, A.; Erlebacher, J. Challenges and opportunities for integrating dealloying methods into additive manufacturing. *Materials.* **2020**, *13*, 3706.

[22] Zhai, Z.;Wang, Y.;Si, C.;Liu, P.;Yang, W.;Cheng, G.; Zhang, Z. Self-templating synthesis and structural regulation of nanoporous rhodium-nickel alloy nanowires efficiently catalyzing hydrogen evolution reaction in both acidic and alkaline electrolytes. *Nano Research.* **2023**, *16*, 2026-2034.

[23] Erlebacher, J.;Aziz, M. J.;Karma, A.;Dimitrov, N.; Sieradzki, K. Evolution of nanoporosity in dealloying. *Nature.* **2001**, *410*, 450-453.

[24] Fujita, T.;Guan, P.;McKenna, K.;Lang, X.;Hirata, A.;Zhang, L.;Tokunaga, T.;Arai, S.;Yamamoto, Y.;Tanaka, N.;Ishikawa, Y.;Asao, N.;Yamamoto, Y.;Erlebacher, J.; Chen, M. Atomic origins of the high catalytic activity of nanoporous gold. *Nature Materials.* **2012**, *11*, 775-780.

[25] Chen, H.;Liang, X.;Liu, Y.;Ai, X.;Asefa, T.; Zou, X. Active site engineering in porous electrocatalysts. *Advanced materials (Deerfield Beach, Fla.).* **2020**, *32*, e2002435.

[26] Luo, M.; Guo, S. Strain-controlled electrocatalysis on multimetallic nanomaterials. *Nature Reviews Materials.* **2017**, *2*, 17059.

[27] Zhang, J.;Mo, Y.;Vukmirovic, M. B.;Klie, R.;Sasaki, K.; Adzic, R. R. Platinum monolayer electrocatalysts for O_2 reduction: Pt monolayer on Pd(111) and on carbon-supported Pd nanoparticles. *The Journal of Physical Chemistry B.* **2004**, *108*, 10955-10964.

[28] Gan, L.;Cui, C.;Rudi, S.; Strasser, P. Core–shell and nanoporous particle architectures and their effect on the activity and stability of Pt ORR electrocatalysts. *Topics in Catalysis.* **2014**, *57*, 236-244.

[29] Chen, S.;Niu, Z.;Xie, C.;Gao, M.;Lai, M.;Li, M.; Yang, P. Effects of catalyst processing on the activity and stability of Pt–Ni nanoframe electrocatalysts. *ACS Nano.* **2018**, *12*, 8697-8705.

[30] Xu, C.;Hao, Q.; Duan, H. Nanoporous pdpt alloy as a highly active electrocatalyst for formic acid oxidation. *Journal of Materials Chemistry A.* **2014**, *2*, 8875-8880.

[31] Li, D.;Meng, F.;Wang, H.;Jiang, X.; Zhu, Y. Nanoporous AuPt alloy with low Pt content: A remarkable electrocatalyst with enhanced activity towards formic acid electro-oxidation. *Electrochimica Acta.* **2016**, *190*, 852-861.

[32] Snyder, J.;McCue, I.;Livi, K.; Erlebacher, J. Structure/processing/properties relationships in nanoporous nanoparticles as applied to catalysis of the cathodic oxygen reduction reaction. *Journal of the American Chemical Society.* **2012**, *134*, 8633-8645.

[33] Oezaslan, M.;Heggen, M.; Strasser, P. Size-dependent morphology of dealloyed bimetallic catalysts: Linking the nano to the macro scale. *Journal of the American Chemical Society.* **2012**, *134*, 514-524.

[34] Heggen, M.;Oezaslan, M.;Houben, L.; Strasser, P. Formation and analysis of core–shell fine structures in Pt bimetallic nanoparticle fuel cell electrocatalysts. *Journal of Physical Chemistry C.* **2012**, *116*, 19073-19083.

[35] McCue, I.;Snyder, J.;Li, X.;Chen, Q.;Sieradzki, K.; Erlebacher, J. Apparent inverse gibbs-thomson effect in dealloyed nanoporous nanoparticles. *Physical Review Letters.* **2012**, *108*, 225503.

[36] Hu, C.;Zhang, Y.;Ren, R.;Xu, J.;Liu, L.;Kong, Q.;Hu, Z.;Zheng, S.;Zhuang, L.;Huang, J.;Tan, Y.; Huang, X. A selenium-mediated layer-by-layer synthetic strategy for multilayered multicomponent nanocrystals. *Nature Synthesis.* **2024**, *3*, 1299-1309.

[37] Timonen, J. V.;Seppälä, E. T.;Ikkala, O.; Ras, R. H. From hot-injection synthesis to heating-up synthesis of cobalt nanoparticles: Observation of kinetically controllable nucleation. *Angewandte Chemie.* **2011**, *50*, 2080-2084.

[38] Casula, M. F.;Jun, Y. W.;Zaziski, D. J.;Chan, E. M.;Corrias, A.; Alivisatos, A. P. The concept of delayed nucleation in nanocrystal growth demonstrated for the case of iron oxide nanodisks. *Journal of the American Chemical Society.* **2006**, *128*, 1675-1682.

[39] Yin, Y.; Alivisatos, A. P. Colloidal nanocrystal synthesis and the organic-inorganic interface. *Nature.* **2005**, *437*, 664-670.

[40] Chen, H. M.;Liu, R.-S.;Lo, M.-Y.;Chang, S.-C.;Tsai, L.-D.;Peng, Y.-M.; Lee, J.-F. Hollow platinum spheres with nano-channels: Synthesis and enhanced catalysis for oxygen reduction. *The Journal of Physical Chemistry C.* **2008**, *112*, 7522-7526.

[41] Yoo, J.;Park, Y.;Choi, J.;Roh, J.;Shin, K.;Cho, H.-S.;Cho, E.;Lee,

C.; Lee, H. M. Electrochemical dealloying of Ni-rich Pt–Ni nanoparticle network for robust oxygen-reduction electrocatalysts. *ACS Sustainable Chemistry & Engineering.* **2023**, *11*, 15460-15469.

[42] Liu, X.-b.;Li, Y.-x.;Zhang, H.-w.;Liu, Y.; Chen, X. Pore structure analysis of directionally solidified porous copper. *China Foundry.* **2020**, *17*, 325-331.

[43] Sun, X.;Zheng, D.;Pan, F.;Qin, C.;Li, Y.;Wang, Z.; liu, Y. 3D nanoporous Ni@NiO/metallic glass sandwich electrodes without corrosion cracks for flexible supercapacitor application. *Applied Surface Science.* **2021**, *545*, 149043.

[44] Seebauer, E. G.; Allen, C. E. Estimating surface diffusion coefficients. *Progress in Surface Science.* **1995**, *49*, 265-330.

[45] Alonso, C.;Salvarezza, R. C.;Vara, J. M. M.;Arvia, A. J.;Vázquez, L.;Bartolomé, A.; Baró, A. M. The evaluation of surface diffusion coefficients of gold and platinum atoms at electrochemical interfaces from combined STM - SEM imaging and electrochemical techniques. *Journal of The Electrochemical Society.* **1990**, *137*, 2161-2166.

[46] Wang, S. C.; Ehrlich, G. Structure, stability, and surface diffusion of clusters: Irx on Ir(111). *Surface Science.* **1990**, *239*, 301-332.

[47] Kyuno, K.; Ehrlich, G. Diffusion and dissociation of platinum clusters on Pt(111). *Surface Science.* **1999**, *437*, 29-37.

[48] Brankovic, S. R.;Wang, J. X.; Adzic, R. R. Metal monolayer deposition by replacement of metal adlayers on electrode surfaces. *Surface Science.* **2001**, *474*, L173-L179.

[49] Li, S.;Shi, M.;Wu, C.;Nie, K.;Wei, Z.;Jiang, X.;Liu, X.;Chen, H.;Tian, X.;Wu, D.; Li, Y. Surface addition of ag on PbO_2 to enable efficient oxygen evolution reaction in ph-neutral media. *Chemical Engineering Journal.* **2024**, *485*, 150043.

[50] Li, Z.;Liu, C.;Abroshan, H.;Kauffman, D. R.; Li, G. $Au_{38}S_2(SAdm)_{20}$ photocatalyst for one-step selective aerobic oxidations. *ACS Catalysis.* **2017**, *7*, 3368-3374.

[51] Wang, J. X.;Inada, H.;Wu, L.;Zhu, Y.;Choi, Y.;Liu, P.;Zhou, W. P.; Adzic, R. R. Oxygen reduction on well-defined core-shell nanocatalysts: Particle size, facet, and Pt shell thickness effects. *Journal of the American Chemical Society.* **2009**, *131*, 17298-17302.

[52] Van der Vliet, D. F.;Wang, C.;Li, D.;Paulikas, A. P.;Greeley, J.;Rankin, R. B.;Strmcnik, D.;Tripkovic, D.;Markovic, N. M.; Stamenkovic, V. R. Unique electrochemical adsorption properties of Pt-skin surfaces. *Angewandte Chemie International Edition.* **2012**, *51*, 3139-3142.

[53] Wang, L.;Gao, W.;Liu, Z.;Zeng, Z.;Liu, Y.;Giroux, M.;Chi, M.;Wang, G.;Greeley, J.;Pan, X.; Wang, C. Core–shell nanostructured cobalt–platinum electrocatalysts with enhanced durability. *ACS Catalysis.* **2018**, *8*, 35-42.

[54] Akin, M.;Bekmezci, M.;Bayat, R.;Kuegou, F. S.;Isik, I.;Kaya, G.; Sen, F. Synthesis of platinum-nickel nanoparticles supported by carbon and titanium oxide structures for efficient and enhanced formic acid oxidation. *Fuel.* **2024**, *373*, 132258.

[55] Di Paola, C.;Plekhanov, E.;Krompiec, M.;Kumar, C.;Marsili, E.;Du, F.;Weber, D.;Krauser, J. S.;Shishenina, E.; Muñoz Ramo, D. Platinum-based catalysts for oxygen reduction reaction simulated with a quantum computer. *npj Computational Materials.* **2024**, *10*, 285.

[56] Yoshinaga, N.;Sugimoto, W.; Takasu, Y. Oxygen reduction behavior of rutile-type iridium oxide in sulfuric acid solution. *Electrochimica Acta.* **2008**, *54*, 566-573.

[57] Gong, B.-T.;Yang, F.-K.;Zhang, Y.-Q.;Li, Y.-W.;Qu, W.-L.;Deng, C.; Wang, Z.-B. Ternary PdCoNi flower-like ultrathin nanosheet assembly with efficient electrocatalytic performance for formic acid oxidation. *International Journal of Hydrogen Energy.* **2025**, *101*, 26-33.

[58] Pei, A.;Ruan, L.;Liu, B.;Chen, W.;Lin, S.;Chen, B.;Liu, Y.;Zhu, L. H.; Chen, B. H. Ultra-low Au decorated PtNi alloy nanoparticles on carbon for high-efficiency electro-oxidation of methanol and formic acid. *International Journal of Hydrogen Energy.* **2020**, *45*, 22893-22905.

[59] Yang, T.;Hou, S.;Xing, J.;Liu, C.;Ge, J.; Xing, W. Formic acid electro-oxidation: Mechanism and electrocatalysts design. *Nano Research.* **2023**, *16*, 3607-3621.

[60] Betts, A.;Briega-Martos, V.;Cuesta, A.; Herrero, E. Adsorbed formate is the last common intermediate in the dual-path mechanism of the electrooxidation of formic acid. *ACS Catalysis.* **2020**, *10*, 8120-8130.

[61] Klinkova, A.;De Luna, P.;Sargent, E. H.;Kumacheva, E.; Cherepanov, P. V. Enhanced electrocatalytic performance of palladium nanoparticles with high energy surfaces in formic acid oxidation. *Journal of Materials Chemistry A.* **2017**, *5*, 11582-11585.

[62] Chen, Y. X.;Heinen, M.;Jusys, Z.; Behm, R. J. Kinetics and mechanism of the electrooxidation of formic acid—spectroelectrochemical studies in a flow cell. *Angewandte Chemie International Edition.* **2006**, *45*, 981-985.

[63] Xia, B. Y.;Wu, H. B.;Li, N.;Yan, Y.;Lou, X. W.; Wang, X. One-pot synthesis of Pt–Co alloy nanowire assemblies with tunable composition and enhanced electrocatalytic properties.

Angewandte Chemie International Edition. **2015**, *54*, 3797-3801.

[64] Wang, W.;Lv, F.;Lei, B.;Wan, S.;Luo, M.; Guo, S. Tuning nanowires and nanotubes for efficient fuel-cell electrocatalysis. *Advanced Materials.* **2016**, *28*, 10117-10141.

[65] Gao, W.;Mueller, J. E.;Jiang, Q.; Jacob, T. The role of Co-adsorbed co and oh in the electrooxidation of formic acid on Pt(111). *Angewandte Chemie International Edition.* **2012**, *51*, 9448-9452.

[66] Courtois, J.;Du, W.;Wong, E.;Teng, X.; Deskins, N. A. Screening iridium-based bimetallic alloys as catalysts for direct ethanol fuel cells. *Applied Catalysis A: General.* **2014**, *483*, 85-96.

[67] Li, Z.;Chen, Y.;Ji, S.;Tang, Y.;Chen, W.;Li, A.;Zhao, J.;Xiong, Y.;Wu, Y.;Gong, Y.;Yao, T.;Liu, W.;Zheng, L.;Dong, J.;Wang, Y.;Zhuang, Z.;Xing, W.;He, C.-T.;Peng, C.;Cheong, W.-C.;Li, Q.;Zhang, M.;Chen, Z.;Fu, N.;Gao, X.;Zhu, W.;Wan, J.;Zhang, J.;Gu, L.;Wei, S.;Hu, P.;Luo, J.;Li, J.;Chen, C.;Peng, Q.;Duan, X.;Huang, Y.;Chen, X.-M.;Wang, D.; Li, Y. Iridium single-atom catalyst on nitrogen-doped carbon for formic acid oxidation synthesized using a general host–guest strategy. *Nature Chemistry.* **2020**, *12*, 764-772.

[68] Li, Y.;Yan, Y.;Yao, M.-S.;Wang, F.;Li, Y.;Collins, S. M.;Chiu, Y.-L.; Du, S. Porous electrodes from self-assembled 3D jointed Pd polyhedra for direct formic acid fuel cells. *Chemical Engineering Journal.* **2023**, *462*, 142244.

[69] Jang, I.;Ahn, M.;Lee, S.; Yoo, S. J. Surfactant assisted geometric barriers on PtNi@C electrocatalyst for phosphoric acid fuel cells. *Journal of Industrial and Engineering Chemistry.* **2022**, *110*, 198-205.

[70] Tan, X. H.;Wang, J. R.;Xiao, Y. H.;Guo, Y. Y.;He, W. D.;Du, B. J.;Cui, H.; Wang, C. X. Engineering topological and chemical disorder in Pd sites for record-breaking formic acid electrocatalytic oxidation. *Advanced Materials.* **2024**, *37*, 2414283.

[71] Wang, M.;Sun, E.;Wang, Y.;Lei, L.;Du, Z.;Zaman, S.;Li, Y.; Wu, M. Oxygen reduction electrocatalyst degradation and mitigation strategies in proton exchange membrane fuel cells. *Applied Catalysis B: Environment and Energy.* **2025**, *367*, 125116.

[72] Sgarbi, R.;Ait Idir, W.;Labarde, Q.;Jourdin, C.;Martin, V.;Andreetta, D.;Wu, P.;Negro, E.;Bassetto, F.;Mainka, J.;Dillet, J.;Marty, C.;Micoud, F.;Noto, V. D.;Kulesza, P.;Lottin, O.; Chatenet, M. Impact of transition metals and electrocatalyst layer thickness on the Pt-based cathodes of proton exchange membrane fuel cells – do multimetallic electrocatalysts necessarily yield an improved performance? *Advanced Energy Materials.* **2024**, https://doi.org/10.1002/aenm.202403212, 2403212.

[73] Vengrenovych, R. D.;Ivanskyy, B. V.;Panko, I. I.;Stasyk, M. O.; Fesiv, I. V. Stability of nanocrystals in 2D and 3D systems in ostwald ripening. *Powder Metallurgy and Metal Ceramics.* **2015**, *54*, 281-291.

[74] Amichi, L.;Yu, H.;Ziabari, A.;Rahman, O.;Arregui-Mena, D.;Hu, L.;Neyerlin, K. C.; Cullen, D. A. A three–dimensional nanoscale view of electrocatalyst degradation in hydrogen fuel cells. *Advanced Energy Materials.* **2024**, *14*, 2402310.

[75] Li, Y.;Hart, J. L.;Taheri, M. L.; Snyder, J. D. Morphological instability in topologically complex, three-dimensional electrocatalytic nanostructures. *ACS Catalysis.* **2017**, *7*, 7995-8005.

[76] Erlebacher, J. Mechanism of coarsening and bubble formation in high-genus nanoporous metals. *Physical review letters.* **2011**, *106*, 225504.

[77] Erlebacher, J.; McCue, I. Geometric characterization of nanoporous metals. *Acta Materialia.* **2012**, *60*, 6164-6174.

[78] Baldizzone, C.;Gan, L.;Hodnik, N.;Keeley, G. P.;Kostka, A.;Heggen, M.;Strasser, P.; Mayrhofer, K. J. J. Stability of dealloyed porous Pt/Ni nanoparticles. *ACS Catalysis.* **2015**, *5*, 5000-5007.

[79] Xia, W.;Gong, M.;Wang, C.;Chen, L.;Wang, Y.;Cai, R.;Liu, Z.;Zhang, M.;Zhang, Q.; Sun, L. Electron tomography reveals porosity degradation spatially on individual Pt-based nanocatalysts. *ACS Applied Materials & Interfaces.* **2022**, *14*, 25366-25373.

[80] Granadillo, L.;Snyder, J.;Xia, Z.; McCue, I. Coarsening kinetics of alloy-doped nanoporous metals. *Scripta Materialia.* **2025**, *255*, 116373.

Electronic Supplementary Material

Surface diffusion-Limited dealloying: A strategy for porosity construction in small-sized alloy nanoparticle electrocatalysts

Siming Li[1,§], Jieyu Zhang[1,§], Suizhu Pei[1], Kangjia Wu[1], Bowen Zhao[1], Min Wang[2] (✉), and Yawei Li[1] (✉)

[1] *School of Chemistry and Chemical Engineering, Shanxi University, Taiyuan 030006, China*
[2] *College of New Energy, China University of Petroleum (Ease China), Qingdao 266580, China*
[§] *Siming Li and Jieyu Zhang contributed equally to this work.*

Supporting information to https://doi.org/10.26599/NR.2025.94907877

Address correspondence to Yawei Li, yaweili@sxu.edu.cn; Min Wang, minwang@upc.edu.cn

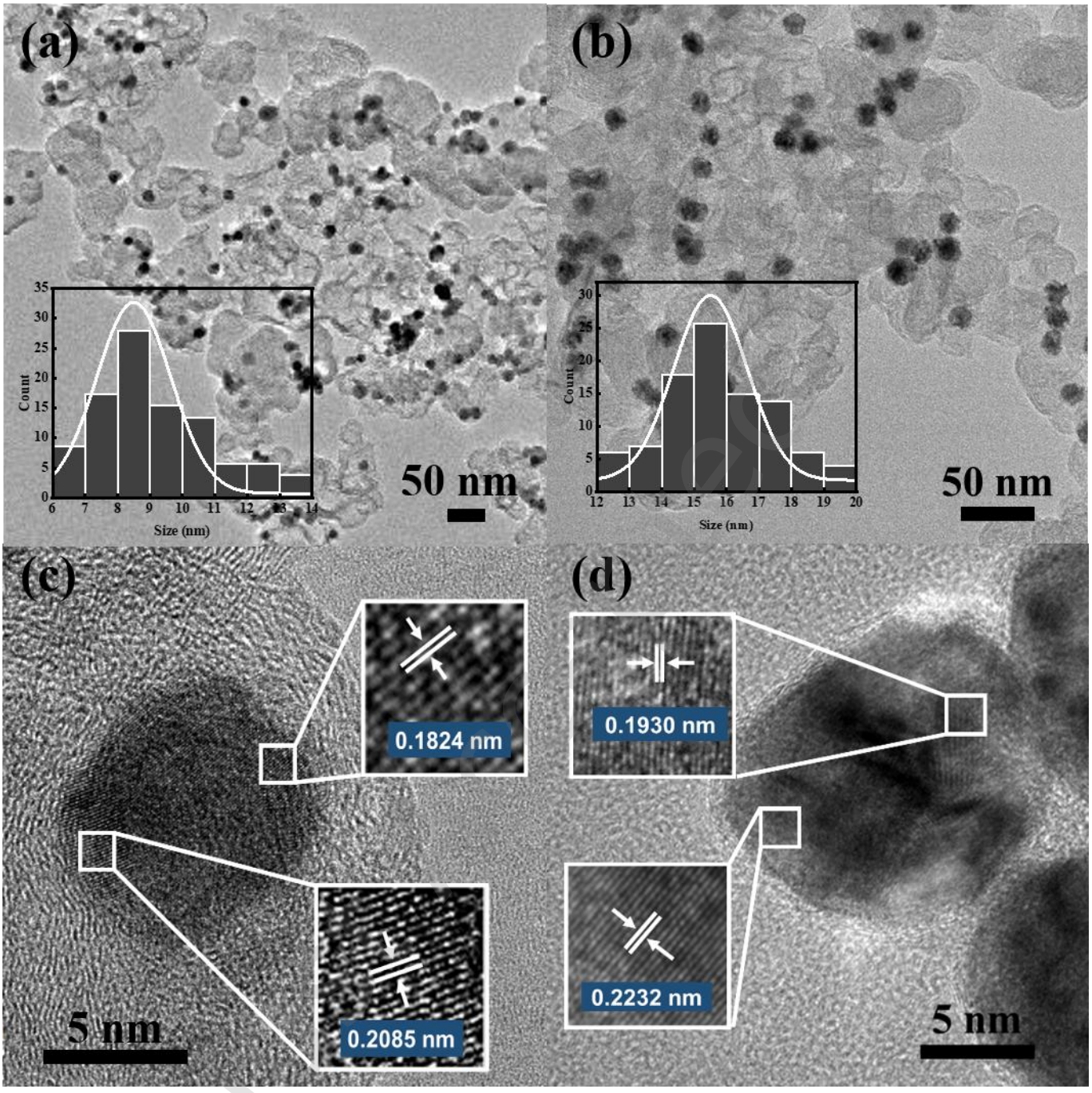

Figure S1 (a) TEM image of 9nm-PtNi. (b) TEM image of 15nm-PtNi. (c) HRTEM image of 9nm-PtNi. (d) HRTEM image of 15nm-PtNi.

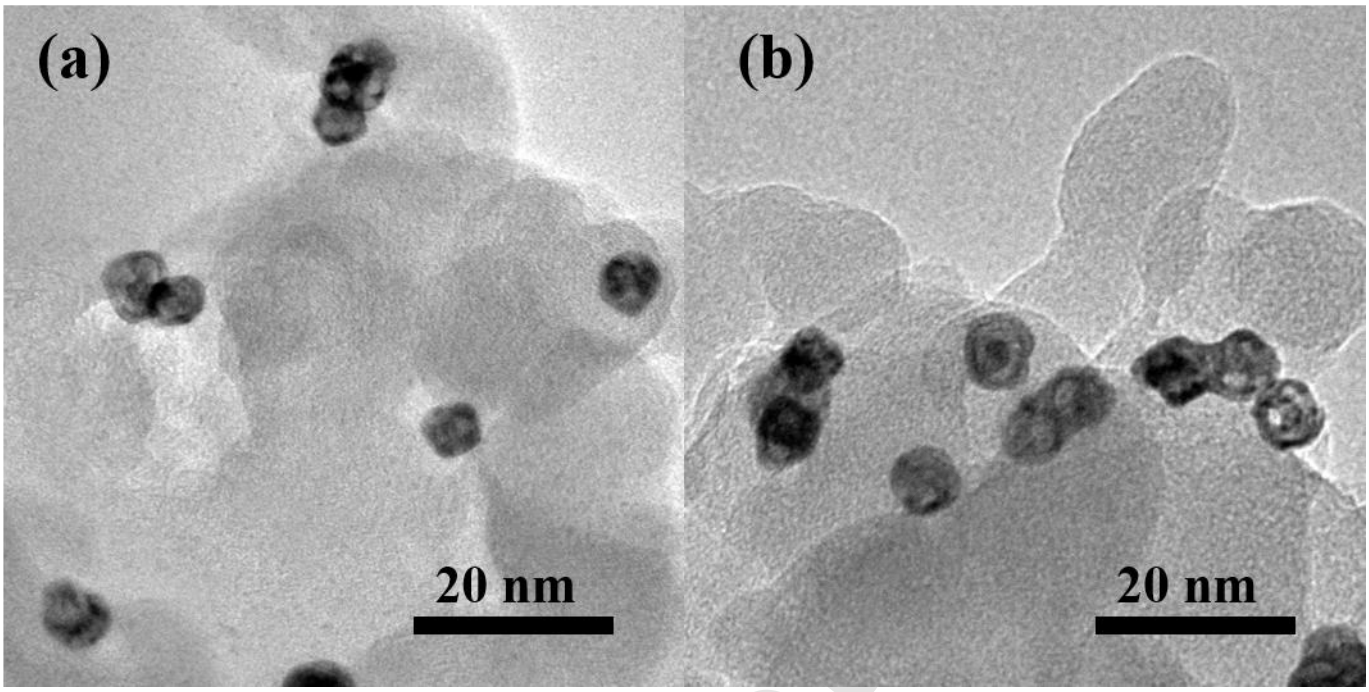

Figure S2 TEM images of 9nm-np-PtNi.

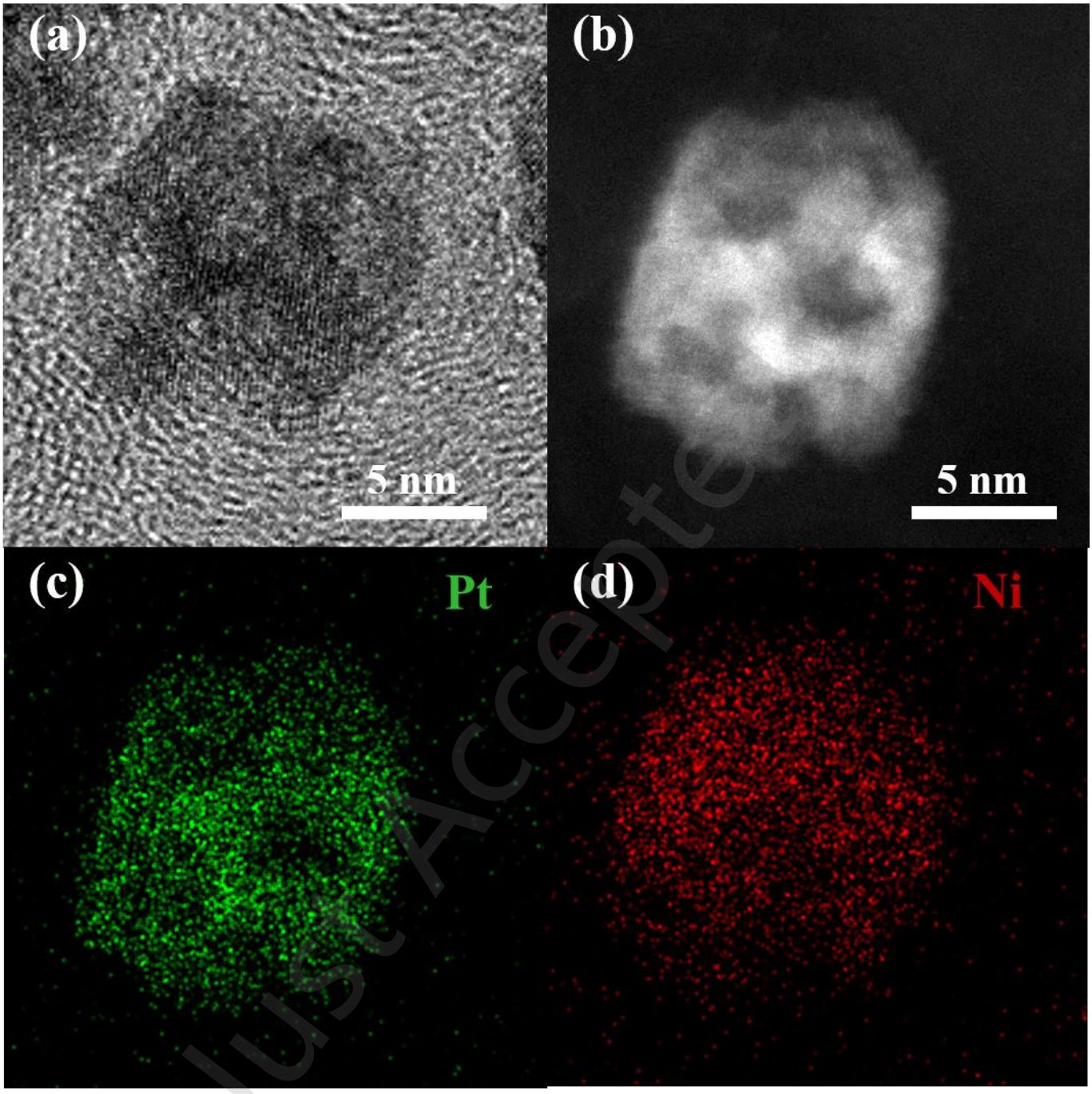

Figure S3 (a) HRTEM image, (b) HAADF-TEM image and the corresponding EDS mapping of (c) Pt and (d)Ni of 15nm-np-PtNi.

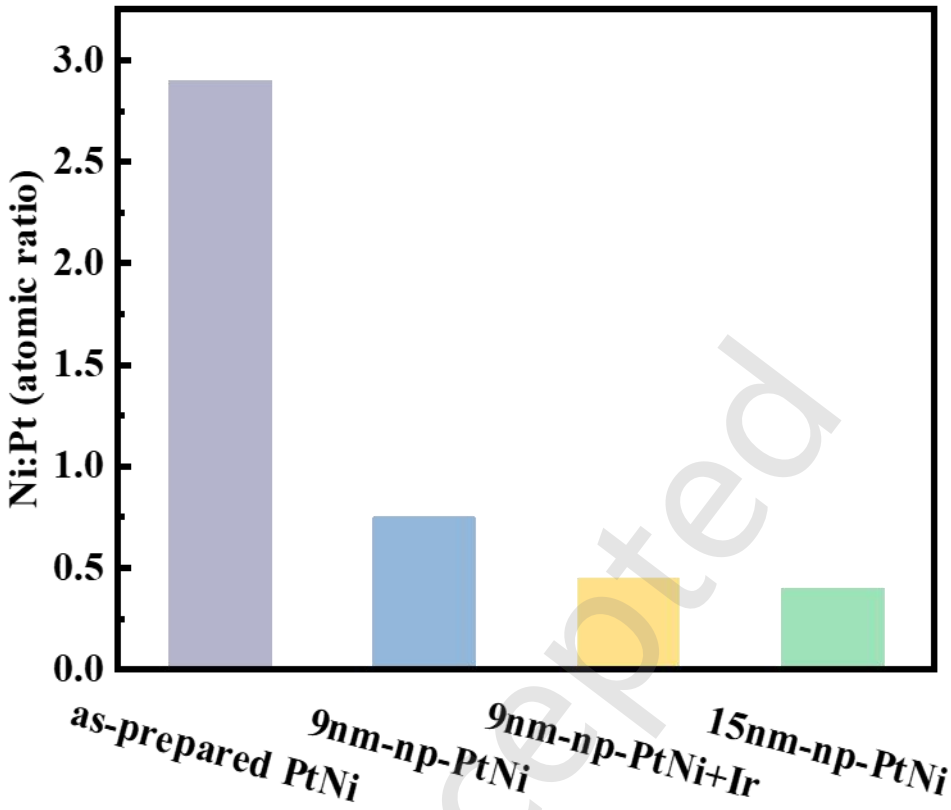

Figure S4 Ni:Pt ratios of EDS results.

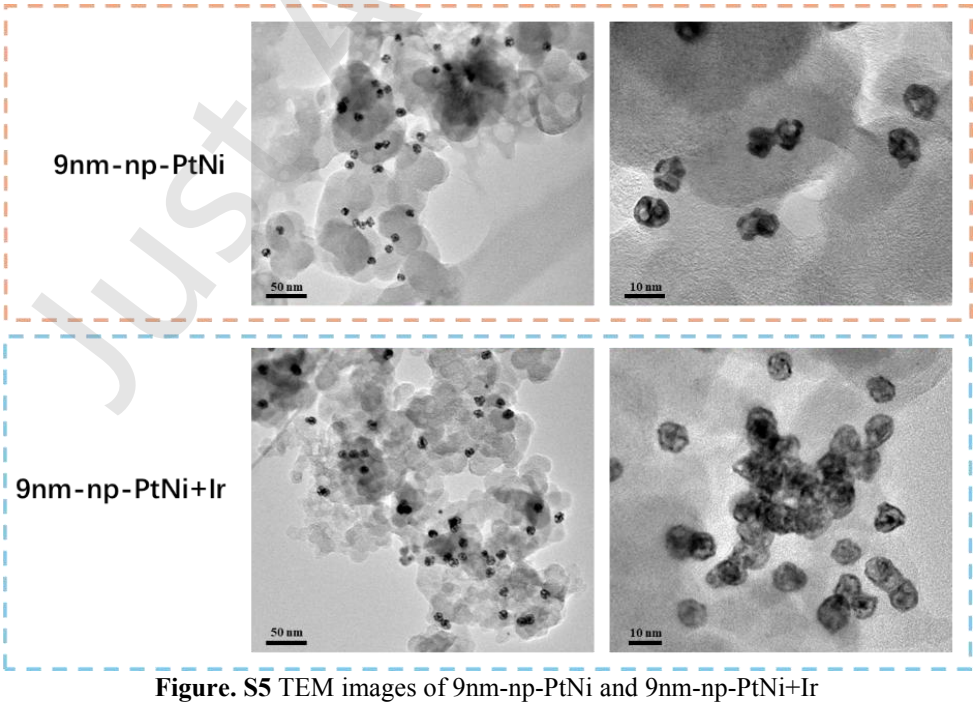

Figure. S5 TEM images of 9nm-np-PtNi and 9nm-np-PtNi+Ir

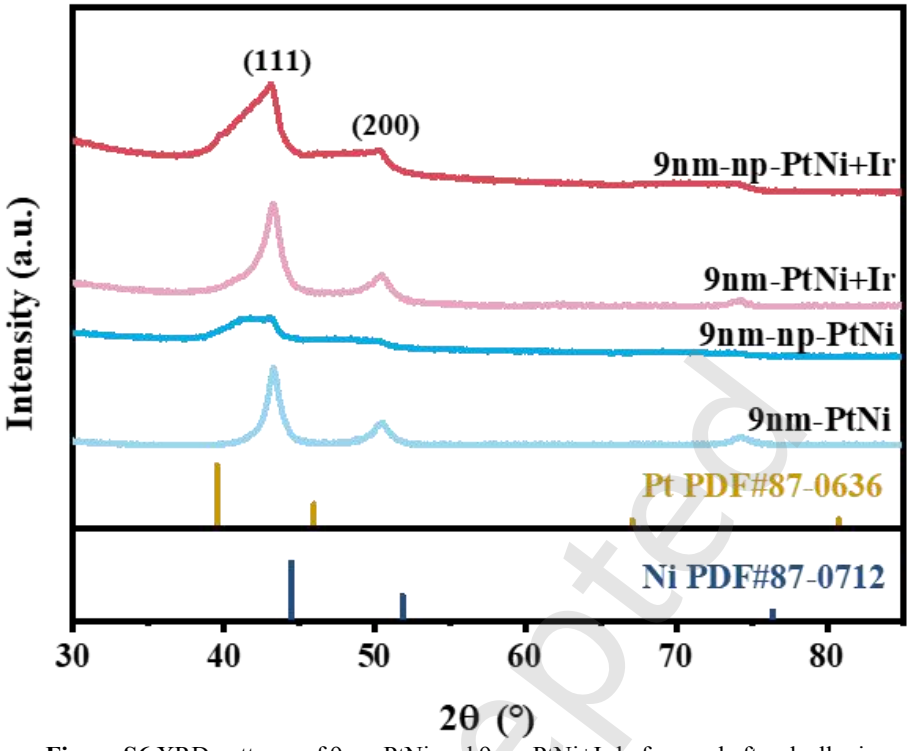

Figure S6 XRD patterns of 9nm-PtNi and 9nm-PtNi+Ir before and after dealloying.

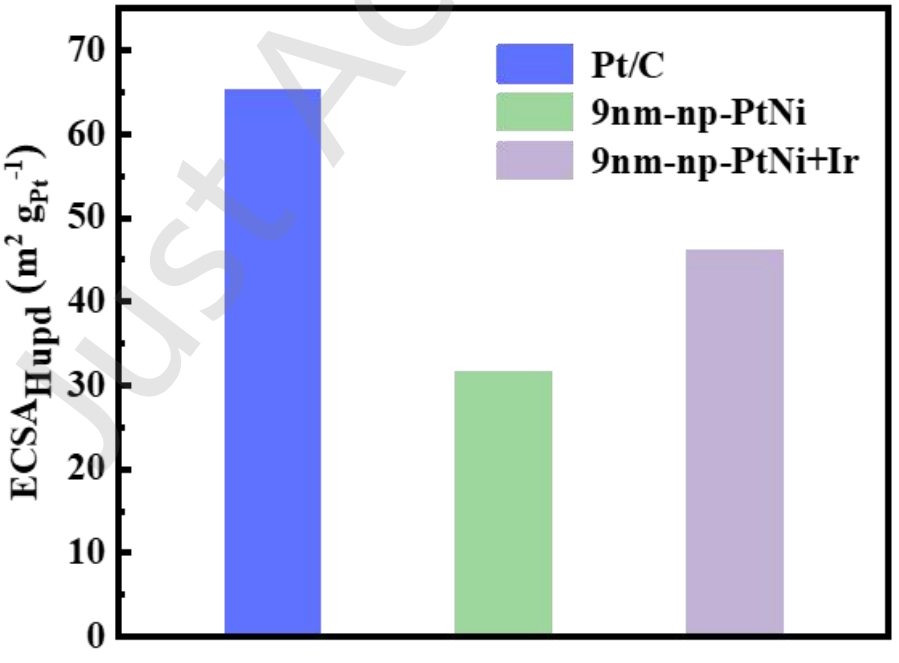

Figure S7 ECSA of Pt/C, 9nm-np-PtNi and 9nm-np-PtNi+Ir.

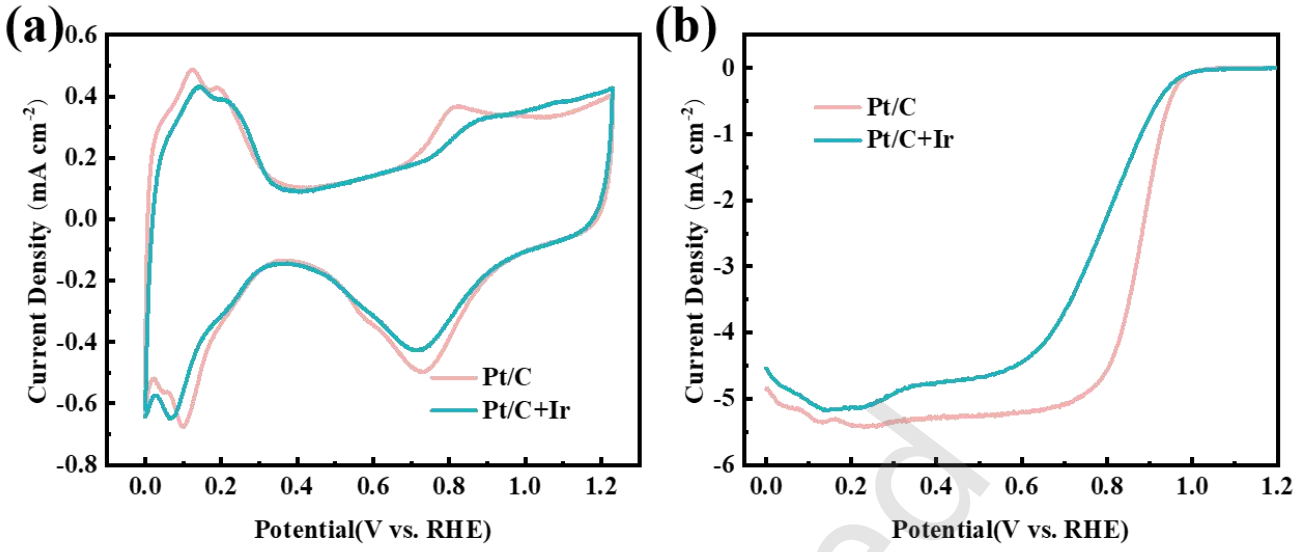

Figure S8 (a) Cyclic voltammograms in Ar-saturated 0.1 M $HClO_4$ at a scan rate of 20 mV s^{-1}. (b) ORR polarization curves in O_2-saturated 0.1 M $HClO_4$ at a rotation rate of 1600 rpm and a scan rate of 20 mV s^{-1}.

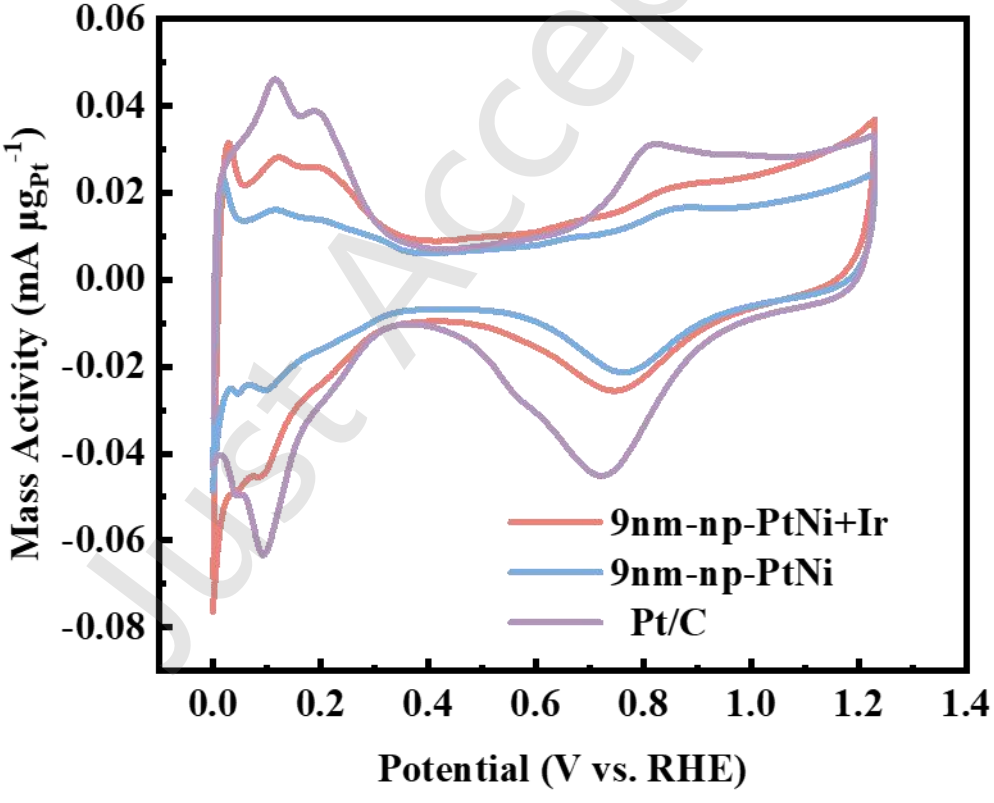

Figure S9 Cyclic voltammograms in Ar-saturated 0.1 M $HClO_4$ at a scan rate of 20 mV s^{-1}.

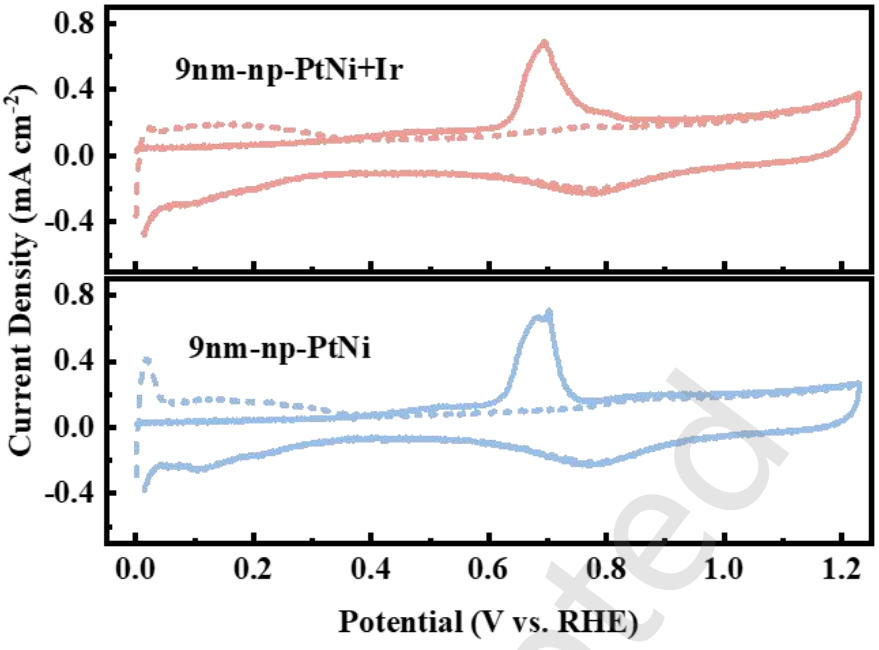

Figure S10 CO stripping curves of catalysts in 0.1 M $HClO_4$ at 20 mV s^{-1}.

Figure S11 XPS spectra of Pt 4f and Ni 2p in 9nm-np-PtNi and 9nm-np-PtNi+Ir.

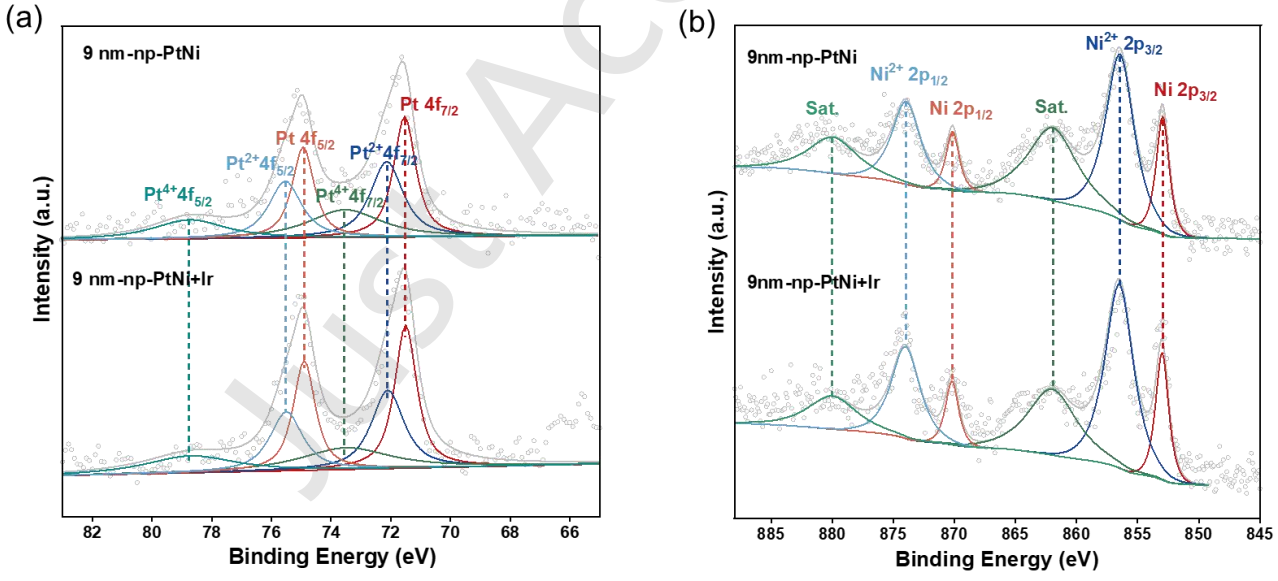

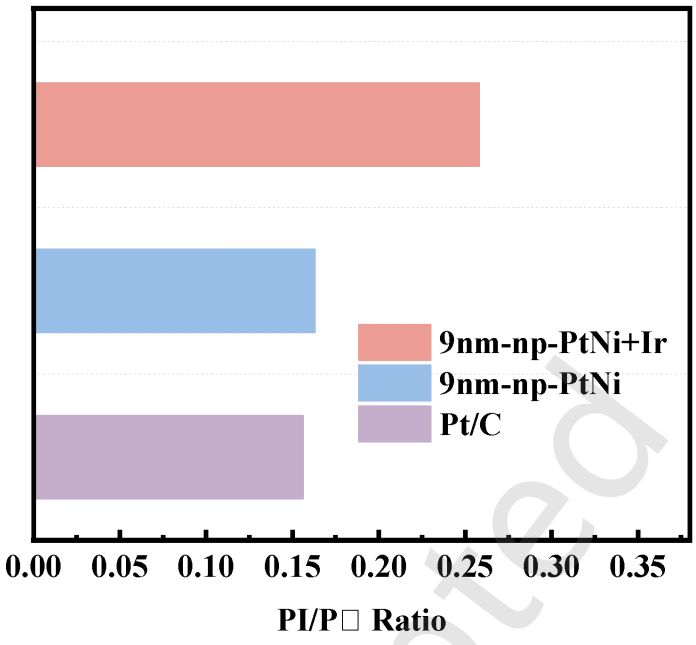

Figure S12 Ratios of Peak I to Peak II of Pt mass-normalized curves of LSV toward FAOR.

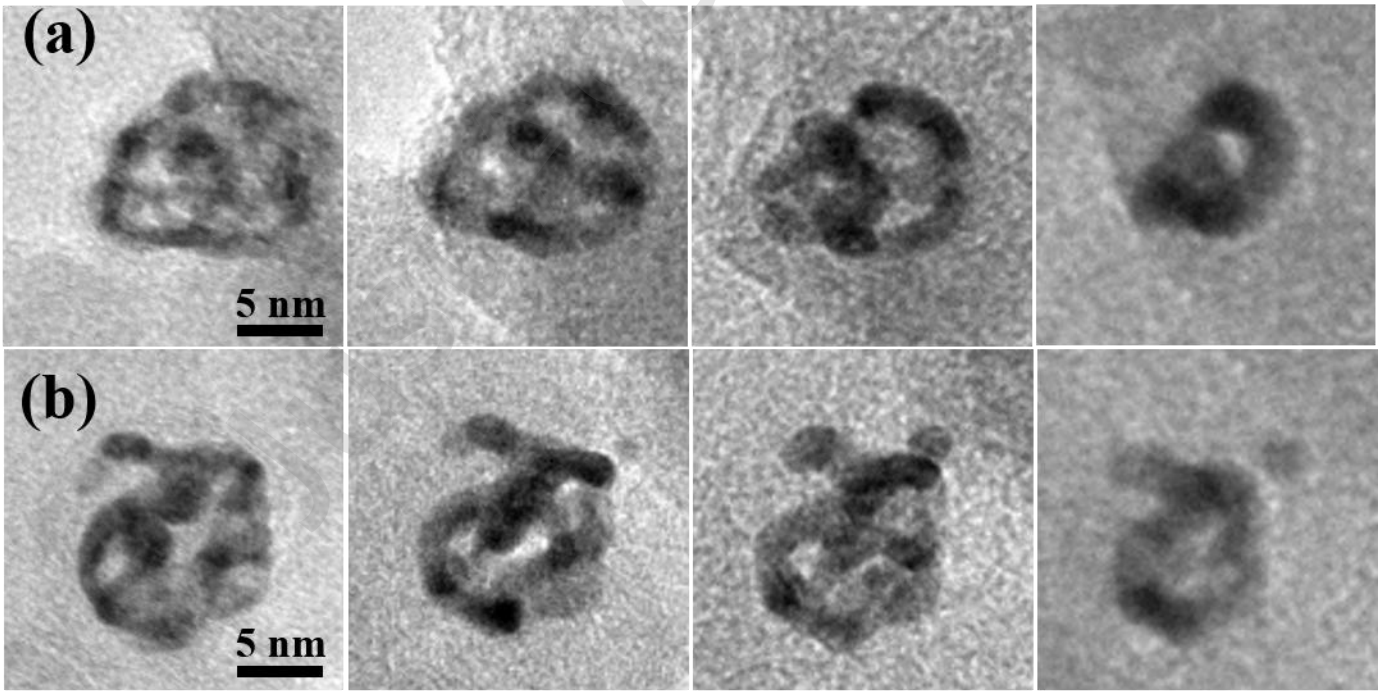

Figure S13 IL-TEM images of single 15nm-np-PtNi particles during ADT.TEM images from left to right represent a0k, 3k, 6k, and 10k potential cycles.

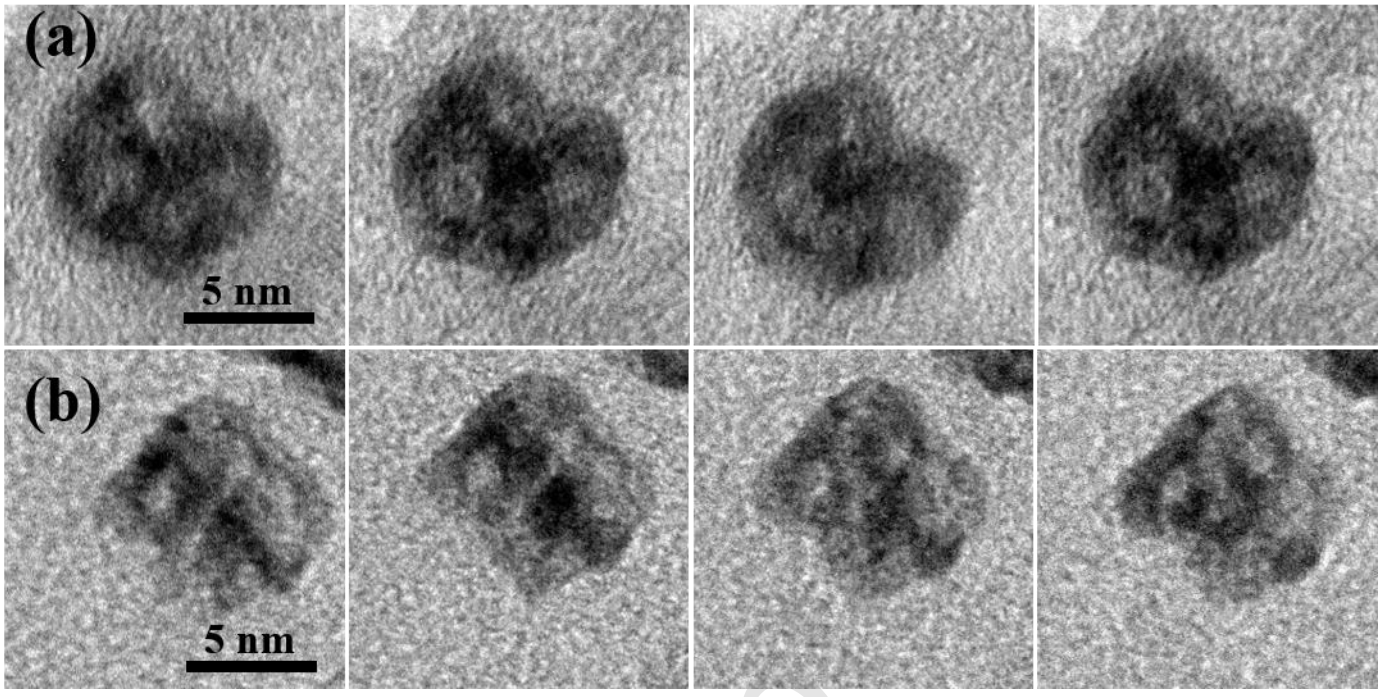

Figure S14 IL-TEM images of single 9nm-np-PtNi+Ir particles during ADT.TEM images from left to right represent 0k, 3k, 6k, and 10k potential cycles.

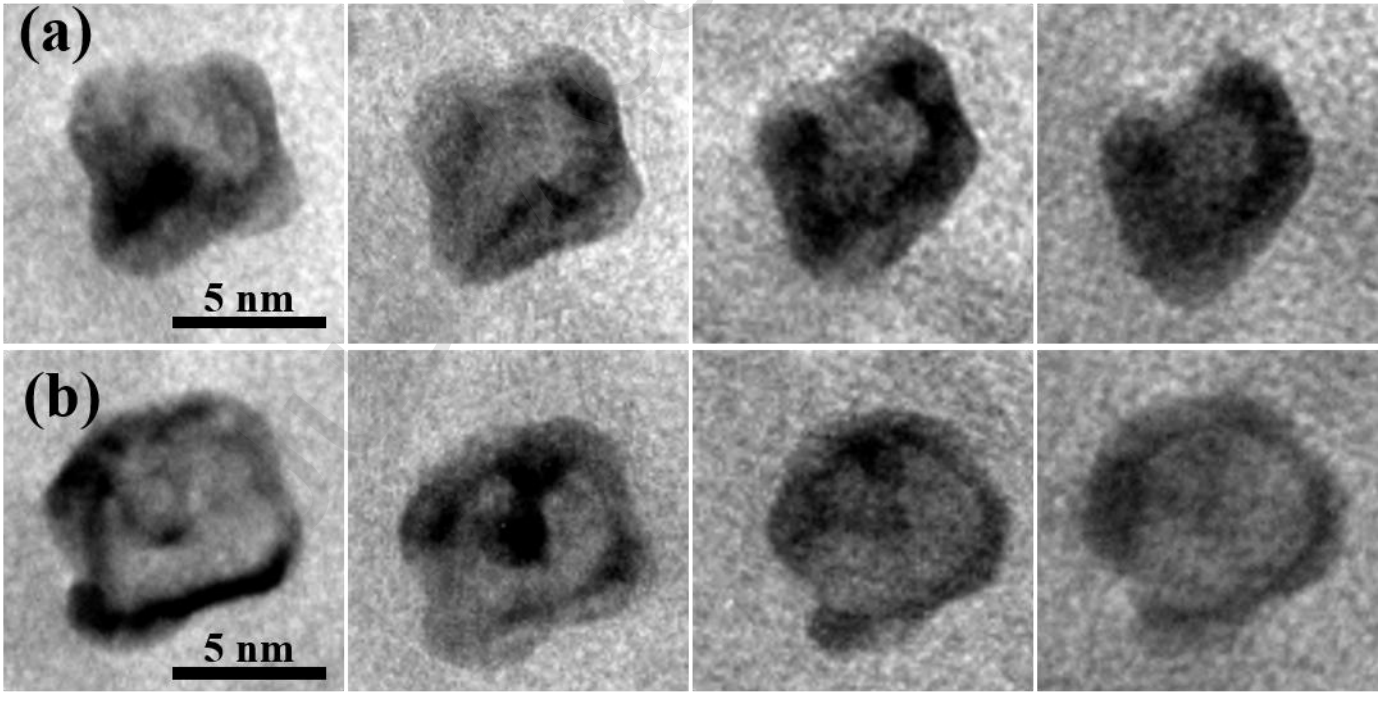

Figure S15 IL-TEM images of single 9nm-np-PtNi particles during ADT.TEM images from left to right represent 0k, 3k, 6k, and 10k potential cycles.

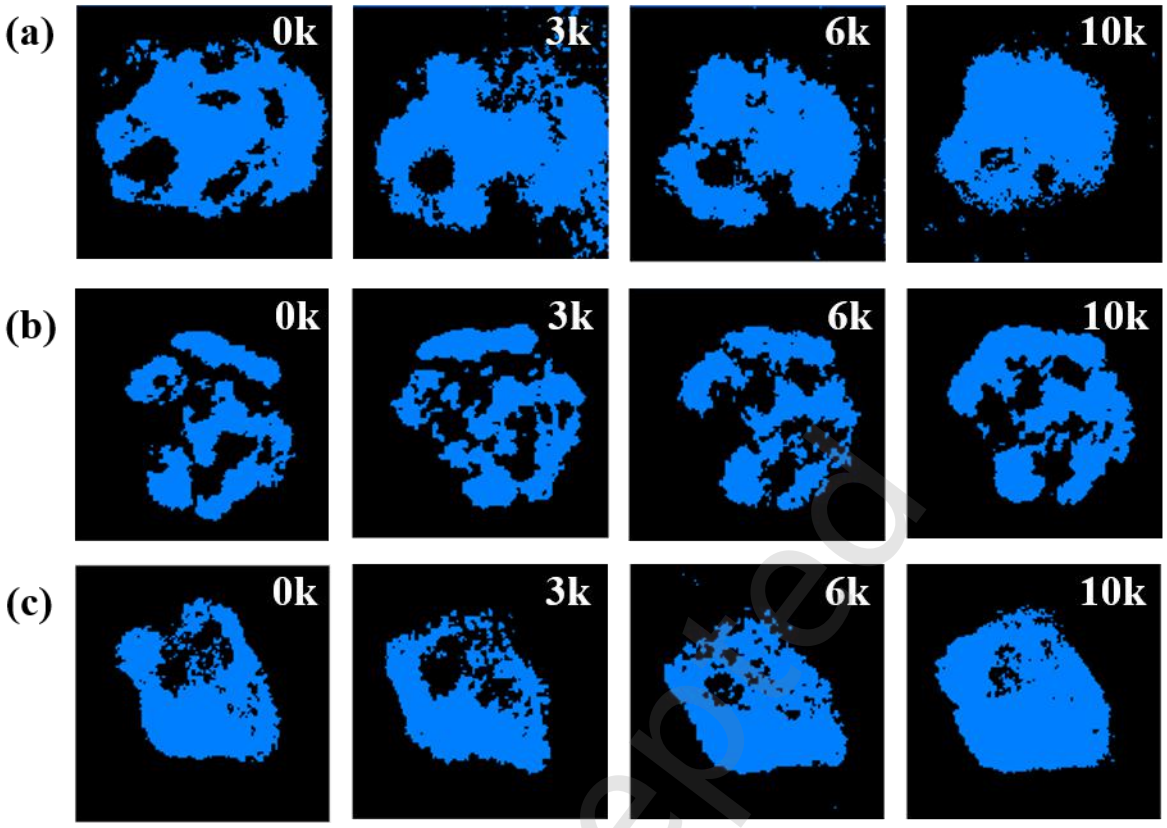

Figure S16 TEM images analyzed by Avizo software of (a) 15nm-np-PtNi particle, (b) 9nm-np-PtNi+Ir particle and (c) 9nm-np-PtNi particle during ADT from left to right represent 0k, 3k, 6k, and 10k potential cycles.

Table S1 Quantitative results of the Ni and Pt on the nanoparticles

Sample	Ni(at.%)	Pt(at.%)	Ni:Pt
as-prepared PtNi	74.36	25.64	2.9:1
9nm-np-PtNi	42.84	57.16	0.75:1
15nm-np-PtNi	28.73	71.27	0.4:1
9nm-np-PtNi+Ir	31.17	69.83	0.45:1

Table S2 ICP-MS results of the 9nm PtNi+Ir catalyst before and after dealloying

Sample	Pt	Ni	Ir	Ir:Pt
as-prepared 9nm-PtNi+Ir	49.5 wt.%	47.81 wt.%	2.69 wt.%	0.0543
9nm-np-PtNi+Ir	84.58 wt.%	11.06 wt.%	4.36 wt.%	0.0515
as-prepared 9nm-PtNi+Ir	23.4 at.%	75.3 at.%	1.3 at.%	0.0556
9nm-np-PtNi+Ir	67.25 at.%	29.23 at.%	3.25 at.%	0.0523

Table S3 XRD analysis of 9nm-PtNi and 9nm-PtNi+Ir before and after dealloying

Sample	Phase Composition	Lattice Parameter	FWHM (111)
9nm-PtNi	Single phase FCC structure	3.610 Å	1.06°
9nm-np-PtNi	Pt-rich FCC structure	3.702 Å	3.55°
9nm-PtNi+Ir	Single phase FCC structure	3.614 Å	1.18°
9nm-np-PtNi+Ir	Pt-rich FCC structure	3.653 Å	2.82°

Table S4 Porosity results calculated by Avizo-based image segmentation method

Sample	0k (%)	3k (%)	6k (%)	10k (%)
15nm-np-PtNi	36.9	30.1	24.7	19.1
9nm-np-PtNi+Ir	38.7	37.9	35.1	32.5
9nm-np-PtNi	25.3	27.3	20.6	18.3